A Study of Stirred Tank Reactor Polymer Electrolyte Membrane Fuel Cell Stack Dynamics

Claire Woo
April 21st, 2006
Advisor: Professor Jay B. Benziger

Submitted in partial fulfillment
Of the requirements for the degree of
Bachelor of Science in Engineering

Department of Chemical Engineering
Princeton University

I hereby declare that I am the sole author of this thesis.

I authorize Princeton University to lend this thesis to other institutions or individuals for the purpose of scholarly research.

Claire Woo

I further authorize Princeton University to reproduce this thesis by photocopying or by other means, in total or in part, at the request of other institutions or individuals for the purpose of scholarly research.

Claire Woo

Princeton University requires the signatures of all persons using or photocopying this thesis. Please sign below, and give address and date.

To my parents who have provided so much for me.
To Cheryl and Jackie who brighten my days.
To friends who have made my time here memorable.

Acknowledgements

I would like to thank Professor Benziger for giving me the opportunity to work on this project, for guiding me patiently along the way, and for his insights day-in and day-out. Next, I would like to thank Warren for everything he has taught me about fuel cells and for helping me get started on the project. I would also like to thank Barclay and James for their assistance and advice in the lab. In addition, I would like to thank Barry and Larry in the SEAS machine shop for their machining skills that made my fuel cell design come to life.

Abstract

A stirred tank reactor design of a polymer electrolyte membrane (PEM) fuel cell was modified and expanded into a stack. Steady-state as well as transient dynamics of the stack at various feed flow rates was examined. Non-uniform distribution of reactants led to differences in individual cell voltages. Instabilities of current and voltages were observed at low feed flow rates, and these could have been due to flooding and limited fuel supply. Starvation of a single cell limited the maximum power that could be generated by the stack. Horizontal surfaces in gas flow channels caused easy build-up of water, leading to a reduction in overall stack performance. In addition, long-term stability of a three-cell stack was demonstrated. A study on water production and removal confirmed that exit gas flow and temperature were important factors in water management in the stack. Over 90% fuel utilization was achieved during control of output current by fuel starvation but periodic instability was observed. Lastly, stainless steel was demonstrated to be unfavorable as a bipolar plate material due to its wetting property.

Table of Contents

1. Introduction

2. Background

3. Experimental Design and Procedures

4. Results and Discussion

5. Conclusions

List of Figures

List of Tables

1. Introduction

1.1 Why Fuel Cells

Amid projections of fossil fuel shortage within the next century and rising concerns about global warming, there is a growing interest in the development of clean alternative energy. Fuel cells have high power density, fast ignition, a long stack life, and water is the only by-product. Among different types of fuel cells, polymer electrolyte membrane (PEM) fuel cells are favored in automobile applications due to their low operating temperatures and quick responses to load changes [1, 2]. Unfortunately, many challenges remain for the wide commercialization of fuel cells. Besides the need to reduce the cost of materials, much remains to be done in terms of understanding the dynamics of fuel cells and optimizing stack design [3]. In addition, stable control of the fuel cell is a difficult problem with inherent tradeoffs and limitations [4].

1.2 Fuel Utilization and Distribution

PEM fuel cells use hydrogen as the fuel and oxygen as the oxidant and generate electric power via an electrochemical reaction. 80% of the hydrogen used nowadays comes from steam reforming, which is a process that produces greenhouse gases. Despite the fact that hydrogen production is still inefficient and expensive, most fuel cells are operated under excess hydrogen feed. In fact, most literature, including Pukrushpan et al. [4], Suh and Steganopoulou [5], and Sun and Kolmanovsky [6] claimed that excess hydrogen and oxygen feed is necessary to avoid operational problems such as stagnant vapor and catalyst degradation. Commercial fuel cells also operate with high stoichiometric hydrogen and air in order to remove the water generated by the redox reaction. So maximum fuel efficiency achieved is only about 50% [7-9].

Surprisingly, few publications have documented the effects of reactant starvation (i.e. 100% utilization of fuel). Natarajan and Nguyen [10] examined the effect of varying hydrogen and oxygen flow rates in a single gas channel PEM fuel cell and found that flooding in downstream segments occurred when humidified feeds were used whereas membrane dehydration in upstream segments became a problem when dry feeds were used. Moreover, when hydrogen was starved, downstream segments suffered significant losses in performance. Scholta et al. [11] observed similar difficulties in maintaining long-term stability of fuel cell stacks due to non-uniform distribution of gases and inhomogeneous cell humidification. With non-uniform distribution, a single starved cell will essentially limit the overall performance of the stack. Thus, uniform reactant distribution is important in flow field design.

1.3 Water Management

The proton conductivity of the membrane in fuel cells depends heavily on water activity. In order to prevent membrane hydration, fuel cells are typically operated with humidified feeds [8, 11, 12]. At the same time, a lot of effort is put into getting rid of the water generated to prevent flooding in flow channels and gas diffusion layers. Nguyan and Knobbe [13] developed a method of sequentially exhausting each cell in the stack so that water was drained from each cell periodically, which also ensured that gas would flow through each cell. Although this method improved performance, it led to a larger and more complex system since it required individual outlets from each cell in the stack and additional electromechanical control devices.

As mentioned in Section 1.2, high stoichiometric gas flow rates are often used to drag out liquid water that is accumulated in the serpentine flow channels that is common in commercial fuel cells [7]. Moreover, the larger the stack, i.e. with more cells connected in series, a larger stoichiometric ratio is required [12]. However, it is counter-intuitive to bring more water into the system by humidifying the reactants when the fuel cell already has difficulty disposing of the water generated by the reaction.

A few different approaches have been attempted to eliminate the need to humidify feeds. Watanabe et al. [14] dispersed catalysts into the membrane to create reaction sites inside the membrane to keep it hydrated. Ge et al. [15] used water-absorbing wicks to keep the anode humidified. These authors either modified the MEA or increased the complexity of the fuel cell in order to solve the paradox of bringing in water while preventing flooding in the system.

There should be a way to use the water generated by the reaction to hydrate the MEA enough so that external humidification of feeds is no long necessary. This will create an auto-humidified system. The advantage of this is not only to simplify the system by getting rid of the humidifying step but also to increase the reactant utilization ratio. With dry feeds, lower flow rates can be employed, which allows for higher reactant utilization and thus a more efficient system. For example, Buchi and Srivinisan [16] attempted to operate fuel cells without any external humidification or modifications to conventional membranes. Back-diffusion of water from cathode prevented the anode from drying out and enabled stable long-term operation, but performance was 20-40% lower than that with fully humidified feeds. Qi and Kaufman [17] used a double-path-type flow-field design that also allowed internal hydration of reactants and membrane for stable long-term operation with dry feeds with only a slight reduction in performance.

Benziger et al. [18] developed a stirred tank reactor PEM fuel cell that could also operate with dry feeds.

1.4 Control of Fuel Cell Power

Typically, the output power of a fuel cell is controlled by a load governor, which varies the external load applied to the fuel cell in order to extract different amounts of power. Pukrushpan et al.[19] built a nonlinear model that described transient responses of power, reactant partial pressures, and membrane hydration by maintaining oxygen flow at a stoichiometric ratio of 2 ($\lambda_{O2} = O_2$ fed/ O_2 reacted = 2). Lauzze and Chmielewski [20] developed a model to simulate PEM fuel cell response to feedback power control by varying the load resistance, cell temperature, relative humidity, and air feed. The complex dynamics of a fuel cell is evident in the complex coupling of control parameters. Golbert and Lewin [21] realized that a sign change in the process gain of power within the normal operating range posed a hurdle to feedback power control.

The response time for this type of load control is fast, but this method not only wastes fuel but also disregards the more intricate changes that occur in the fuel cell, including changes in temperature, relative humidity, membrane conductivity, all of which affect output at a longer response time. One of the motivations behind this thesis is to investigate the feasibility of an alternative control method - fuel starvation control.

Using the stirred tank reactor (STR) PEM fuel cell design by Benziger et al. [18], previous work had demonstrated successful current control of a single fuel cell by fuel starvation. 100% hydrogen utilization was proved possible. Although stoichiometric feeds of hydrogen and oxygen were demonstrated to be infeasible for stable control, the need for oxygen was reduced to only 30% excess, as opposed to 100% excess proposed by most publications [1, 7, 8, 22, 23]. Control by fuel starvation not only improves fuel efficiency but also simplifies the control system and eliminates the need for additional infrastructure for recycling excess fuel.

1.5 Thesis Objective

This thesis uses the unique STR PEM fuel cell design by Benziger et al. [18] to study water management as well as fuel starvation in a fuel cell stack. The design for a single STR fuel cell was modified and expanded into a stack with individual cells connected in series. Performance at different flow conditions was examined and analyzed for a two-cell stack and a three-cell stack. Particular attention was paid to water balance and transport in the overall system. Long-term stability was briefly studied. Feasibility of current control in a stack by fuel starvation was investigated. Lastly, stainless steel was compared to graphite as an alternative bipolar plate material.

2. Background

2.1 How Fuel Cells Work

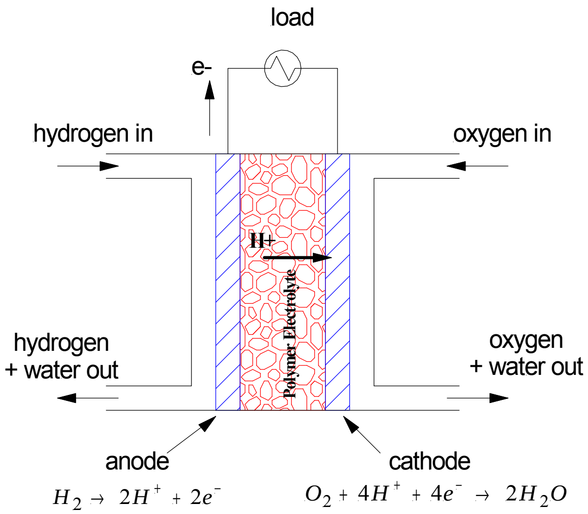

Figure 2.1 Schematic of a PEM fuel cell. Hydrogen enters the gas flow channels, where it is absorbed onto the anode surface and is catalytically oxidized into protons and electrons via the reaction shown on the bottom left. Protons diffuse across the polymer electrolyte membrane whereas electrons pass through an external load. Oxygen absorbed onto the cathode surface reacts with the crossover protons and electrons to produce water via the reaction shown on the bottom right.

Fuel cells are electrochemical devices that derive electricity from chemical energy. In this sense, they are similar to batteries, except that in fuel cells there is a continuous flow of reactants and products in and out of the device. Figure 2.1 shows the schematic of a PEM fuel cell that uses hydrogen as fuel and oxygen as oxidant. Hydrogen enters the gas flow channels and is absorbed onto the anode surface where it is catalytically broken down into protons and electrons. Protons diffuse across the membrane while electrons are driven through an external load. Protons and electrons meet again at the cathode, where they react with oxygen to produce water. The overall reaction is shown in Equation 2.1, where $\Delta G^o = -232$ kJ/mol.

$$H_2(g) + \frac{1}{2}O_2(g) \rightarrow H_2O(g) \tag{2.1}$$

Within the fuel cell, in addition to this chemical reaction, several coupled processes take place at the same time, including the diffusion of reactants across the electrodes, diffusion of protons across the membrane, heat generation and removal, water production at the cathode, and water transport through and out of the fuel cell. The rates of the reaction and these transport processes determine the dynamics of the fuel cell. These processes are dependent on the quality of the membrane-electrode assembly (MEA), flow field designs, and operating conditions (reactant flow rates, temperature, pressure etc.), all of which affect the overall performance of the fuel cell and thus are important aspects to consider in fuel cell design and operation.

2.2 Circuit Equivalence

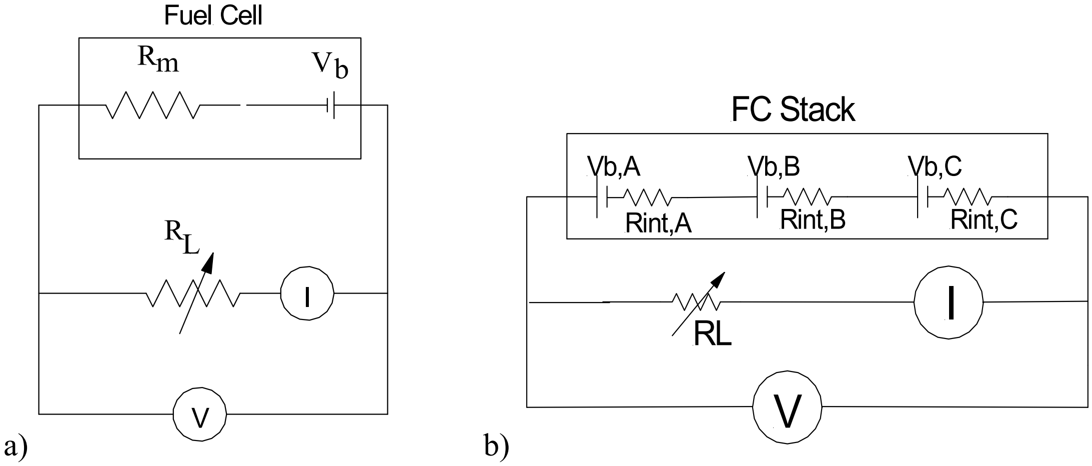

Figure 2.2 a) Equivalent circuit of a single fuel cell. V_b represents the chemical potential difference across the fuel cell electrodes. R_{int} is the internal resistance of the fuel cell that is mostly dependent on the MEA. R_L is the external load resistance. b) Equivalent circuit of a three-cell stack.

The fuel cell system can be represented as an electric circuit, as shown in Figure 2.2. The battery voltage, V_b, signifies the chemical potential difference between the anode and cathode in the fuel cell. Chemical potential is represented by the activity of hydrogen at the electrode/electrolyte surface. The hydrogen activity at the anode interface is determined by a balance between the partial pressure of hydrogen in the gas flow channels, the diffusion of hydrogen through the gas diffusion layer, and rate of the consumption of hydrogen by the reaction at the interface. The hydrogen activity at the cathode is determined by assuming equilibrium with oxygen and water. Taking into account mass transfer and consumption rate, the battery voltage can be expressed as Equation 2.2. Terms and variables are defined in Table 2.1 at the end of this section.

$$V_b = -\frac{\Delta G^o}{4F} + \frac{RT}{4F}\ln\left[\frac{\left(P_H - \frac{i}{2Fk_A}\right)^2\left(P_o - \frac{i}{2Fk_c}\right)}{\left(\frac{P_w^{cathode}}{P_w^o}\right)^2 P_{total}^3}\right] \tag{2.2}$$

Besides the partial pressures of hydrogen and oxygen, the battery voltage is dependent on water activity at the cathode. However, the logarithmic dependence of V_b on water vapor pressure is less significant compared to the effect of water on membrane resistance (see Section 2.4). k_A and k_C are mass transfer coefficients that are functions of electrode porosity, pore tortuosity, electrode thickness, and gas diffusivity, which is also highly dependent on water content in electrode.

The battery voltage is the potential difference that drives an ionic current through the membrane-electrode assembly that has an internal resistance R_{int}, while at the same time forcing an electric current through an external load resistance R_L. Under typical operating range of the fuel cell, R_L regulates the current in the fuel cell by controlling the flow of protons and electrons through the circuit. Under a finite load, the circuit in Figure 2.2a can be described by Equation 2.3. Current is determined by the battery voltage and the two resistances, as shown in Equation 2.4. The equivalent circuit for a fuel cell stack in series is shown in Figure 2.2b. V_b in Equation 2.3 becomes the sum of individual battery voltages, and R_{int} becomes the sum of individual internal resistances. Equation 2.3 can be expanded into Equation 2.5.

$$V = V_b - iR_{\text{int}} \tag{2.3}$$

$$i = \frac{V_b}{R_{\text{int}} + R_L} \tag{2.4}$$

$$V = \sum_k V_{b,k} - i \sum_k R_{\text{int},k} \tag{2.5}$$

2.3 Voltage Losses

Figure 2.3 shows a typical IV curve (also called polarization curve) that is obtained by varying the external load to the fuel cell. Ideally, without any voltage loss, a hydrogen fuel cell can achieve a voltage of 1.2V at 60°C, as shown by the solid line obtained by modeling a 1.3cm^2 PEM fuel cell using Equations 2.2-2.4. But the ideal voltage of 1.2V could almost never be achieved due to crossover of hydrogen through the membrane into the cathode.

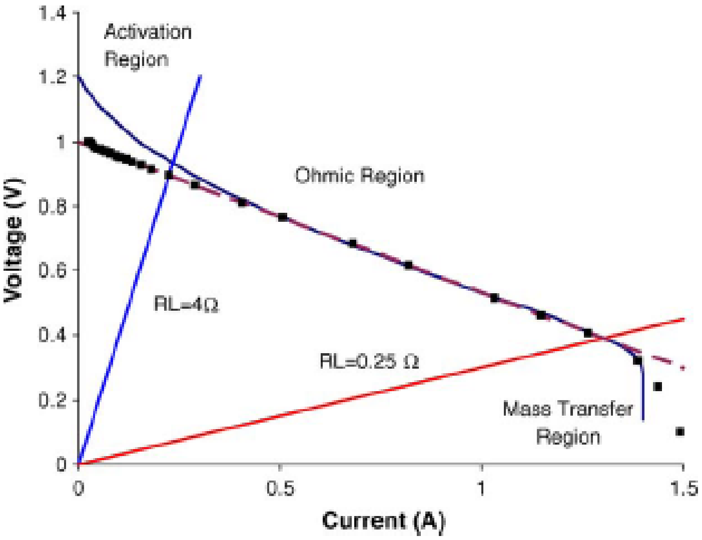

Figure 2.3 Typical IV curve for a fuel cell [24]. The symbols are experimental data from a 1.3cm^2 PEM fuel cell whereas the solid line is obtained by modeling the fuel cell using Equations 2.2-2.4. In the activation region, voltage is lost through driving electrons through the barrier in the electrodes. Voltage drop in the ohmic region is mainly caused by internal resistance of the MEA. In the mass transfer region, current cannot increase further because rate of diffusion of reactants to the catalyst surface has reached its maximum limit.

At open circuit (i.e. infinite load resistance and zero current), voltage is usually between 0.9-1.0V, which represents the difference in chemical activity of hydrogen between the anode and cathode. At finite load resistance, Figure 2.3 shows 3 operating ranges of the fuel cell. The activation region has current less than 0.2A cm^{-2}, which is typically the case when load is larger than 4Ω. Voltage is lost from driving the chemical reaction through an electron transfer barrier on the electrode surface.

In the ohmic region, where R_L typically ranges from 0.25Ω to 4Ω, current is mainly limited by the resistance of the MEA to ion flow. This resistance is affected by the water content in the membrane as well as the 3-phase interface between the electrodes, the catalyst, and the membrane. The ohmic region is the most common operating range of the fuel cell. According to Equation 2.3, R_{int} can be determined from the negative slope of the ohmic region of the IV curve, and the y-intercept of is V_b.

At low loads and high current density, the fuel cell reaches the mass transfer region where voltage loss is associated with limitations in diffusion of reactants from the gas flow channels to the electrode surface where the thin layer of catalyst is located. In this region, due to the lower external resistance, high current is possible. However, rate of consumption of reactants is limited by the rate of diffusion across the gas diffusion layers, thus setting a maximum limit on current that can be produced by the fuel cell. This effect is included in Equation 2.2 which expresses battery voltage as a function of partial pressures of reactants, current, and mass transfer coefficients.

All these voltage drops can be summarized by Equation 2.6a-b, where *A and b* are constants dependent on the electrode material and cell conditions. Equation 2.6b shows that activation losses become significant only when current is small.

$$V = V_b - \Delta V_{activation} - iR_{\text{int}} \tag{2.6a}$$

where $$\Delta V_{activation} = A \ \ln\left(\frac{i}{b}\right) \tag{2.6b}$$

2.4 The Importance of Water

One key factor determining the success or failure of fuel cell operation is water management. Water transport through the polymer electrolyte membrane is dependent on the electro-osmotic drag of water by protons as well as the back diffusion of water due to a concentration gradient between the anode and cathode [25]. Water is important because the level of hydration in the membrane determines the proton conductivity of the membrane, which in turn affects the current and voltage of the fuel cell, as expressed in Equation 2.3 and 2.4. Neglecting temperature dependence, the resistivity of a Nafion membrane typically used in fuel cells can be described by Equation 2.7 [26], where a_w is water activity in the membrane.

$$R_m = 10^7 \exp[-14(a_w)^{0.2}] \ \Omega \ cm \tag{2.7}$$

When water activity is low, the resistivity of the membrane will increase, which consequently makes R_{int} bigger. On the other hand, gas diffusion in the electrodes is also dependent on water activity. When there is too much water present, the gas diffusion layer becomes over-saturated, and water will condense. Liquid water blocks the diffusion of reactants from gas flow channels to the catalyst surface, a phenomenon known as flooding. In effect, this reduces the active surface area of membrane and lowers cell performance. The ideal is to maintain 80-100% relative humidity in the fuel cell so that the membrane is considerably hydrated while the diffusion layers are not so saturated that liquid water blocks gas diffusion.

Overall mole balance of water in a fuel cell can be described by Equation 2.8, where N_w^m is the water content in the membrane in terms of moles.

$$\frac{\partial N_w^m}{\partial t} = \left(\frac{Q_A^{in} P_w^{A,in}}{RT} + \frac{Q_C^{in} P_w^{C,in}}{RT} \right) - \left(\frac{Q_A^{out} P_w^{A,out}}{RT} + \frac{Q_C^{out} P_w^{C,out}}{RT} \right) + \frac{i}{2F} \qquad (2.8)$$

The terms in the first bracket on the right hand side take in to account water brought in by feeds, and the terms in the second bracket is the amount of water removed by effluent convection. The last term on the right is moles of water produced per ampere of current generated. Water balance is complicated by intermediate processes of water transport from cathode catalyst surface across the membrane and gas diffusion layer into the gas flow channels. At steady-state, mass transfer of water from the membrane/catalyst interface to gas flow channels can be described by Equations 2.9 and 2.10 shown below, where k_w^A and k_w^C are mass transfer coefficients of water across the gas diffusion layers of anode and cathode respectively.

$$\frac{Q_A^{out} P_w^{A,out}}{RT} = k_w^A (P_w^{membrane} - P_w^{A,out}) \qquad (2.9)$$

$$\frac{Q_C^{out} P_w^{C,out}}{RT} = k_w^C (P_w^{membrane} - P_w^{C,out}) \qquad (2.10)$$

2.5 Current Control by Fuel Starvation

Equation 2.11 is the overall mole balance of hydrogen in the fuel cell. At 100% H_2 utilization, if pure hydrogen feed is used, no hydrogen should exit the cell, so Q_A^{out} is zero. At steady-state, Equation 2.11 simplifies to Equation 2.12, which formed the basis for the analysis of hydrogen starvation control studies. Similarly, Equations 2.13 and 2.14 describe the oxygen mole balance used for the case of oxygen starvation.

$$\frac{V_A}{RT}\frac{\partial P_{H_2}^{out}}{\partial t} = \left(\frac{Q_A^{in} P_{H_2}^{in}}{RT} - \frac{Q_A^{out} P_{H_2}^{out}}{RT} \right) - \frac{i}{2F} \tag{2.11}$$

$$\frac{i}{2F} = \frac{Q_A^{in} P_{H_2}^{in}}{RT} \tag{2.12}$$

$$\frac{V_C}{RT}\frac{\partial P_{O_2}^{out}}{\partial t} = \left(\frac{Q_C^{in} P_{O_2}^{in}}{RT} - \frac{Q_C^{out} P_{O_2}^{out}}{RT} \right) - \frac{i}{2F} \tag{2.13}$$

$$\frac{i}{2F} = \frac{Q_C^{in} P_{O_2}^{in}}{RT} \tag{2.14}$$

Using Equations 2.12 as the government equation, current control of a single STR fuel cell by fuel starvation had been achieved. 100% hydrogen utilization was proved possible, and Figure 2.4 shows that stable control was maintained at various temperatures. For a current setpoint change from 0.3A to 0.4A, the response time was under 10 seconds. When H_2 flow was stopped for 5s, current dropped but was able to return to setpoint value within 32-54s. A change in load caused a slight disturbance, but current was able to recover within 7-14s.

As shown in Figure 2.5, stoichiometric feeds of hydrogen and oxygen led to unstable current. However, if oxygen excess was raised to 30%, current was able to remain stable. This 30% O_2 excess ratio was maintained for the current control tests shown in Figure 2.4. The control is believed to be achieved by a dynamic balance between the pressure in the cell and the water reservoir accumulated in the cell. During fuel starvation, a vacuum was created in the gas flow chambers in the fuel cell. Since gas outlets were submerged in water baths, the larger atmospheric pressure pushed water into the fuel cell, as shown by the schematic in Figure 2.6. The presence of liquid water blocked active MEA area, which was directly related to internal resistance. So a change in water reservoir level in effect led to a change in internal resistance, which in turn affected the output current. This was hypothesized to be the control mechanism at work during current control by fuel starvation.

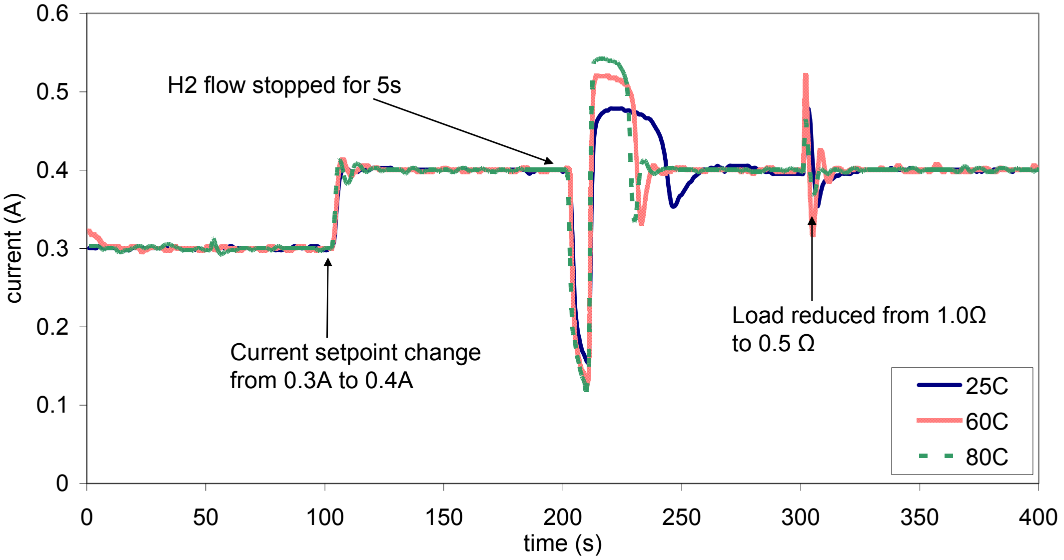

Figure 2.4 Three different disturbance tests performed at 25°C, 60°C, and 80°C in a single STR PEM fuel cell under H_2 starvation control. 100% H_2 was utilized, and 30% excess O_2 was supplied. For a setpoint change, the process time was less than 10s for all 3 temperatures. When H_2 flow was stopped for 5s, current was able to return to setpoint value within 32-54s. When load was reduced from 1Ω to 0.5Ω, current had a slight disturbance but was able to recover within 7-14s.

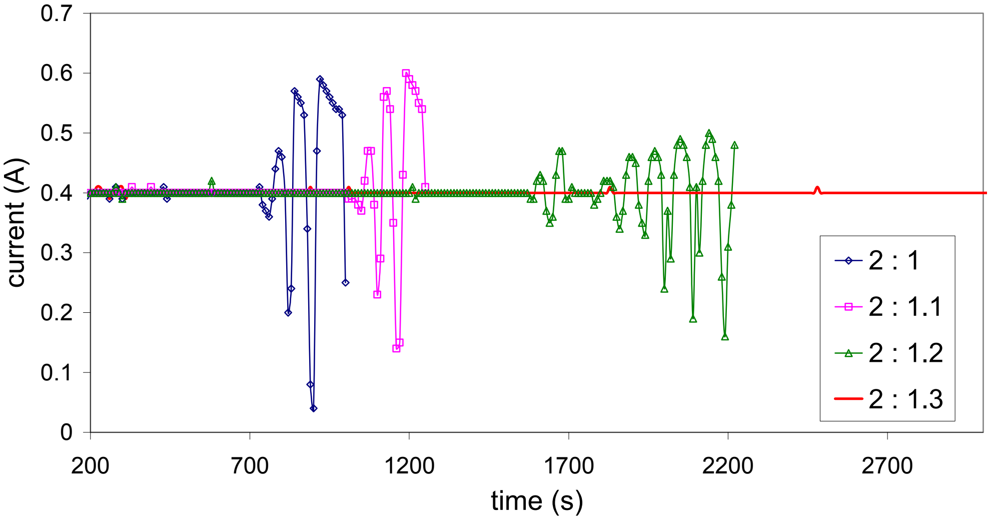

Figure 2.5 Transient current at different ratios of H_2:O_2 flows. Legend indicates the ratio of H_2:O_2 feeds. Stability was maintained only when at least 30% excess O_2 was supplied.

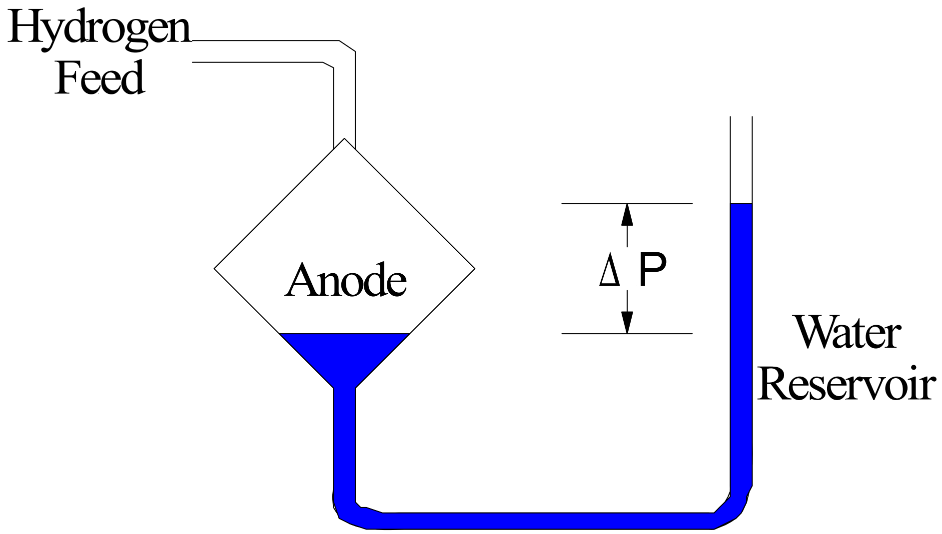

Figure 2.6 Schematic of the fuel cell anode connected to an external water bath and the accumulation of an internal water reservoir. Water blocks active MEA area, which causes a decrease in internal resistance. The water flows in and out of the anode to maintain the total pressure in the gas flow channel equal to the external pressure. This is believed to be the mechanism of control by fuel starvation in the STR fuel cell.

Control by fuel starvation not only improves fuel efficiency but also simplifies the control system and eliminates the need for additional infrastructure for recycling excess fuel. However, if changing the internal water reservoir level is indeed the control mechanism in the STR fuel cell, the control is expected to be more difficult in a stack due to non-uniform fuel distribution. Uneven distribution of fuel will lead to earlier starvation of downstream cells which then becomes the bottleneck in overall stack performance. However, if a clever manifold is constructed to ensure uniform distribution of feeds to each cell, control by fuel feed in a stack may theoretically be possible.

Symbol	Definition
a_w	water activity
F	Faraday's constant, 96,500 [C mol^{-1}]
ΔG^o	standard free energy change [kJ mol^{-1}]
i	current through external load [A]
k_A	mass transfer coefficient for H_2 from anode channel to anode surface [A bar^{-1}]
k_C	mass transfer coefficient of O_2 from cathode channel to cathode surface [A bar^{-1}]
k_w	mass transfer coefficient of water across gas diffusion layers
N_w^m	water content in membrane [mol]
P_H	partial pressure of hydrogen [bar]
P_O	partial pressure of oxygen [bar]
P_w	partial pressure of water [bar]
Q_A^{in}	volumetric flow rate of H_2 feed to anode [cm^3 min^{-1}]
Q_A^{out}	volumetric flow rate of H_2 exiting anode [cm^3 min^{-1}]
Q_C^{in}	volumetric flow rate of O_2 feed to cathode[cm^3 min^{-1}]
Q_C^{out}	volumetric flow rate of O_2 exiting cathode[cm^3 min^{-1}]
R	universal gas constant, 83.14 [bar cm^3 K^{-1} mol^{-1}]
R_{int}	internal resistance of fuel cell stack [Ω]
$R_{int,k}$	internal resistance of individual cell [Ω]
R_L	load resistance [Ω]
R_m	membrane resistance [Ω]
T	fuel cell stack temperature [K]
V_b	fuel cell battery voltage [V]
V_k	voltage across each individual cell [V]
V_{total}	voltage measured across external load [V]

Table 2.1 Nomenclature used in this section and in all following sections.

3. Experimental Design and Procedures

3.1 Fuel Cell Stack Design

Figure 3.1a shows the two-cell stack used for most of the tests conducted. A schematic of the stack is shown in Figure 3.1b. The stack consists of two individual cells, cell A and cell B, which are connected in series. For the three-cell stack, cell C is added to the right of cell B. Gas flow channels were carved out of graphite bipolar plates. Gas flow channel patterns are shown in Figure 3.2. The contact area between the pure gas phase and the MEA was 2.2 cm^2. In each cell, H_2 and O_2 enter at the top of the anode and cathode chamber respectively. Unused reactants exit at the bottom together with the water produced.

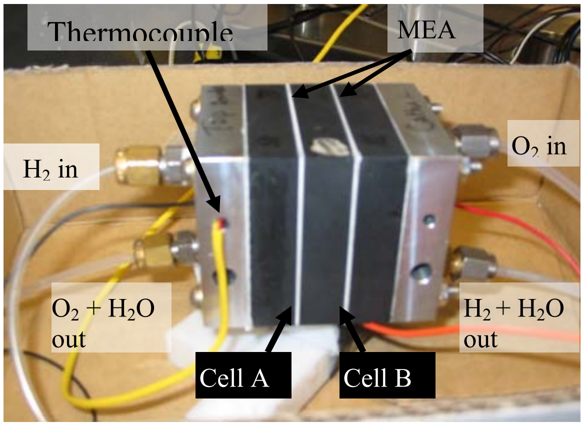

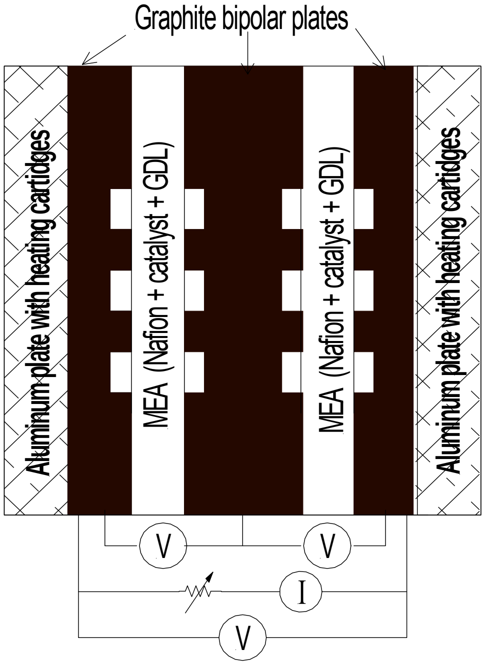

Figure 3.1a (top) Fuel cell stack mainly made out of graphite and aluminum. It consists of two individual cells and 2 MEAs. Inlet and outlet positions are indicated. Figure 3.1b (right) Schematic of the fuel cell stack with electric connections drawn in.

This unique design was devised previously in the Benziger research group to make use of gravity as a means to drain excess water generated in the redox reaction. As shown in Figure 3.2, there are no horizontal surfaces in the gas flow chambers. The gas outlets on both sides of the stack also slope downward to facilitate water drainage. However, the channels connecting the individual cells were horizontal, thus allowing water to accumulate in between cells. The design is based on coupled stirred tank reactors coupled through a membrane [18]. The residence times of the reactants in the gas flow channels ($V/Q \sim 1.2$-12s) are larger than the characteristic diffusion time ($V^{2/3}/D \sim 0.3$-1 s) at flow rates of $Q \sim 1$-20 mL/min. This ensures that gas compositions at anode and cathode gas chambers are uniform, which satisfies the definition of a continuous stirred tank reactor.

To prevent gas leaks during operation, the stack was sealed at the 4 corners using stainless steel bolts wrapped in hollow Teflon rods (see Figure 3.2). Teflon rods were used to keep the aluminum and graphite blocks electrically insulated and thus prevented short circuit.

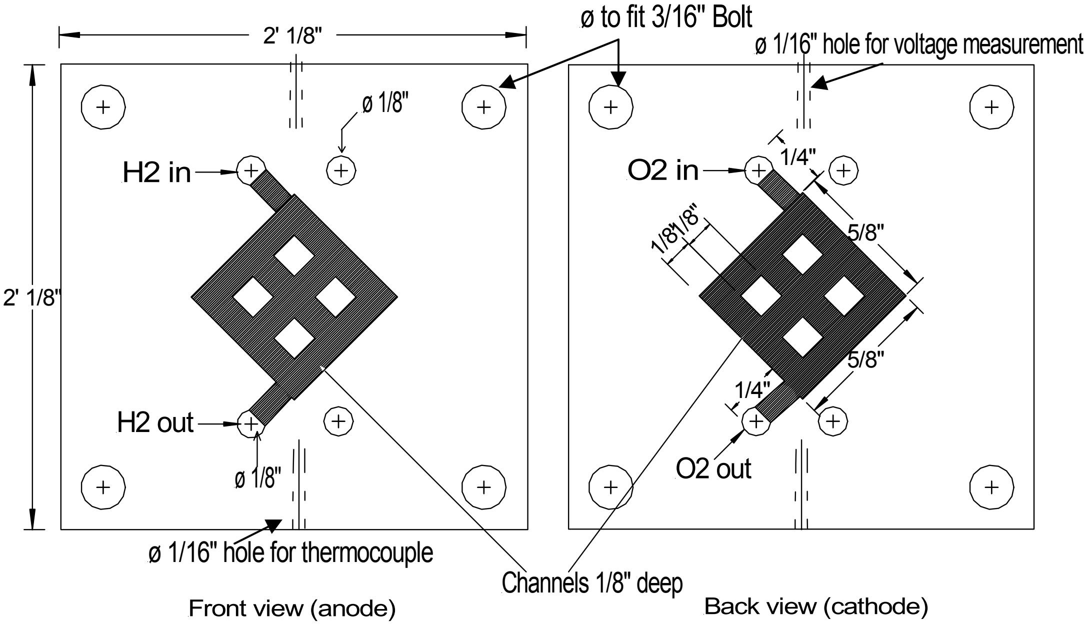

Figure 3.2 Design of the gas flow channels in the fuel cell stack. The left panel corresponds to the anode flow channels, and the right panel corresponds to the cathode flow channels. They are mirror images of each other. The block is made of graphite. A membrane-electrode assembly (MEA) is placed in between two of these graphite blocks. Dimensions are shown in inches. A 1/16" hole was carved out of the top of the graphite plate for individual cell voltage measurements.

Figure 3.3 shows the schematic of the side graphite plate, copper current collector, gasket insulator, and aluminum block. Copper foil current collectors were placed between the graphite block and aluminum block at each end. These current collectors are connected to the external load, forming the external electric circuit. A rubber gasket was placed between the copper foil and aluminum for insulation. A thermocouple and 2 heating rods were placed in the aluminum blocks for temperature control.

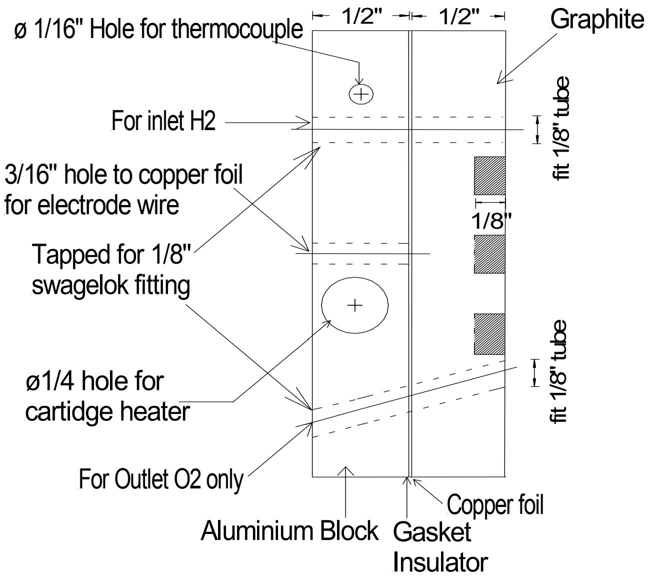

Figure 3.3 Schematic of side graphite plates and aluminum blocks with copper current collector and gasket insulator placed in between the two blocks. Heating rods were placed in the aluminum blocks at both ends of the stack.

An equivalent circuit of the fuel cell stack setup was shown in the previous section in Figure 2.2b. In the experimental setup, the external load R_L was manually controlled and changed by a simple variable resistor externally connected to the fuel cell stack. Total voltage drop across the stack was determined by measuring the voltage difference across electric wires connected to current collectors. Individual cell voltages, V_A, V_B, and V_C, were measured by inserting electric wires into holes at the top of the graphite plates and measuring the voltage drop across these plates (see Figure 3.2).

Current was determined by measuring the voltage drop across a sensing resistor of 0.1Ω parallel to the external load applied. Current can then be calculated by dividing the differential voltage by 0.1Ω. Individual cell voltages and total voltage drop were logged by the LabTech Notebook program through a data acquisition board (CyberResearch Inc, CYDAS 08 Series). Internal resistances are calculated by measuring the negative slope of the ohmic region of the IV curve.

3.2 Stainless Steel as Bipolar Plates

Graphite was initially chosen as the material for bipolar plates. However, it was observed that gas leaked out of the graphite blocks. Stainless steel, which is less permeable to gas than graphite is, was chosen as a comparison material. Figure 3.4 shows the fuel cell stack with stainless steel bipolar plates. Table 3.1 shows some of the thermal and electrical properties of these two materials. Since stainless steel is much denser than graphite, ¼" thick stainless steel plates were used, in comparison to ½" thick graphite plates. The depth of the gas flow channels was reduced from 1/8" in the graphite plates to 1/16" in the stainless steel plates. Despite reduced thickness, the stainless steel stack still weighted considerably more than the graphite stack.

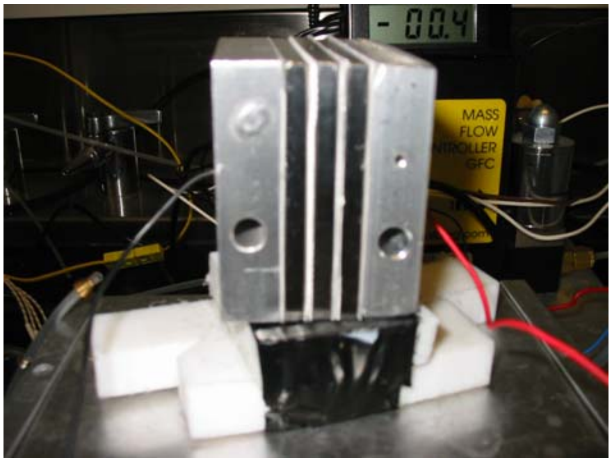

Figure 3.4 Fuel cell stack with stainless steel bipolar plates. It has the same schematic and flow channel patterns as shown in Figure 3.1b and 3.2. But the depth of gas flow channels are only 1/16", compared to 1/8" deep channels in the graphite stack.

Property	Graphite	Stainless steel (Type 316)
Density [g/cm^3]	2.25	8
Thermal conductivity [W/m-K]	24	16.3
Electrical resistivity [Ω-cm]	6e-3	7.4e-5

Table 3.1 Comparison of electrical and thermal properties of graphite and stainless steel.

3.3 MEA preparation

The membrane used in all the tests was Nafion^{TM} 115, a perfluorosulfonated polymer (Ion Power Inc, Bear, DE). The Nafion membrane was cleaned by the standard procedure of sequential boiling for 1 hr each in 3wt% H_2O_2, DI water, 1M sulfuric acid, and DI water respectively. The MEA used for testing consisted of a Nafion 115 membrane pressed between 2 E-tek electrodes (A6 ELAT), which were carbon cloths coated on one side with a Pt/C catalyst. Catalyst weight loading was 0.5mg Pt/cm^2. The electrodes were brushed with 5wt% Nafion solution to a loading of 0.6mg Nafion/cm^2 before pressing with the membrane. The MEA was prepared by hot pressing the Nafion membrane between the 2 electrodes at 140^{o}C at 40MPa for 90 seconds. The MEA was sealed with rubber gaskets. A sample MEA is shown in Figure 3.5 below. After each MEA was hot pressed, it was stored in 100% relative humidity environment for at least 3 hours before it was placed in the fuel cell stack for testing.

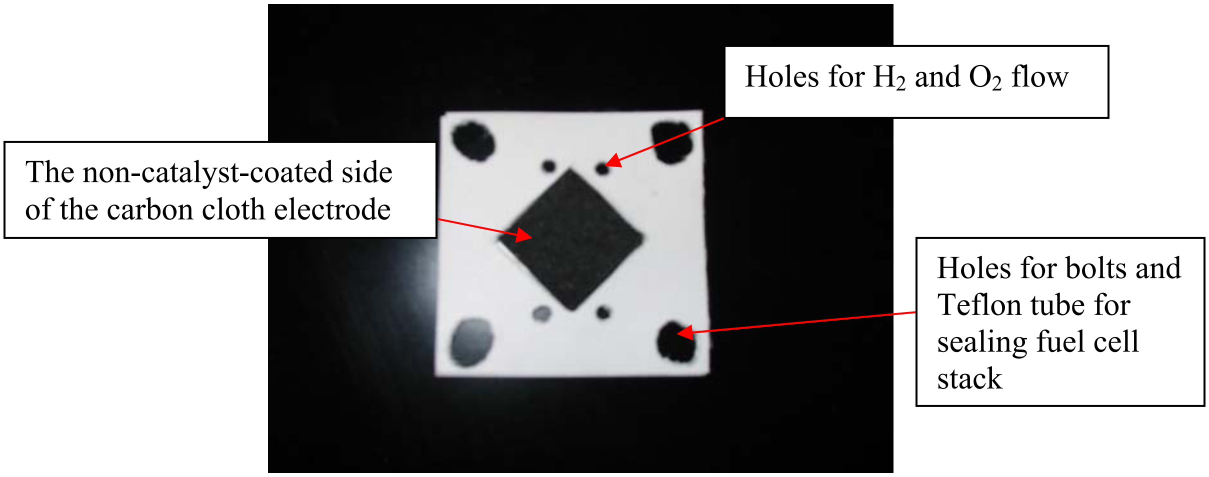

Figure 3.5 Sample MEA used in fuel cell stack testing

Different MEAs were used for different sets of data presented in the next section. Because MEAs were individually pressed and were not custom-made, different MEAs had significant variations in performance. Since the objective was to study general behavior of the fuel cell stack, MEA quality was not optimized. Thus, when analyzing test results, trends within one set of data were identified, but comparison of absolute values of different sets of data was avoided.

3.4 Fuel Cell Stack Operation

Dry H_2 and O_2 feeds from commercial cylinders (Airgas, Inc.) were fed into the stack in a counter-current flow pattern. H_2 was first fed into the anode chamber of cell A and then into the anode of cell B, whereas O_2 was first fed into the cathode of cell B and then into that of cell A. As shown in Figure 3.6, H_2 and O_2 flow in opposite directions. O_2 flows in opposite direction of the current, thus named the counter-current flow.

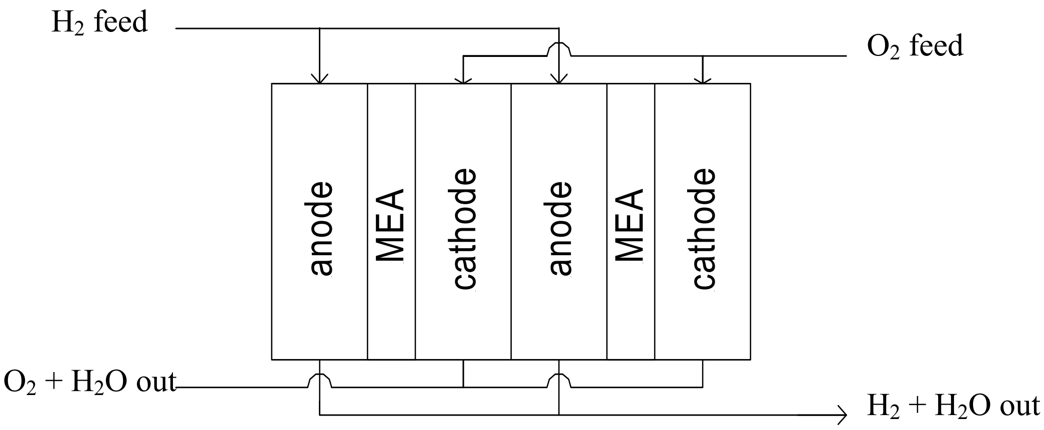

Figure 3.6 Schematic of counter-current flow of gases in the two-cell stack

A feedback control loop was set up LabTech Notebook program to control reactant gas flow rates via remote control of GFC Mass Flow Controllers (Aalborg Instruments). PID control parameters were optimized for the gas flow controllers. Effluent tubes from the fuel cell were submerged in water baths at room temperature to prevent back-diffusion of air as well as to collect water from the anode and cathode. This was also useful for observing gas bubbles exiting the stack in order to determine whether the stack was under starvation condition.

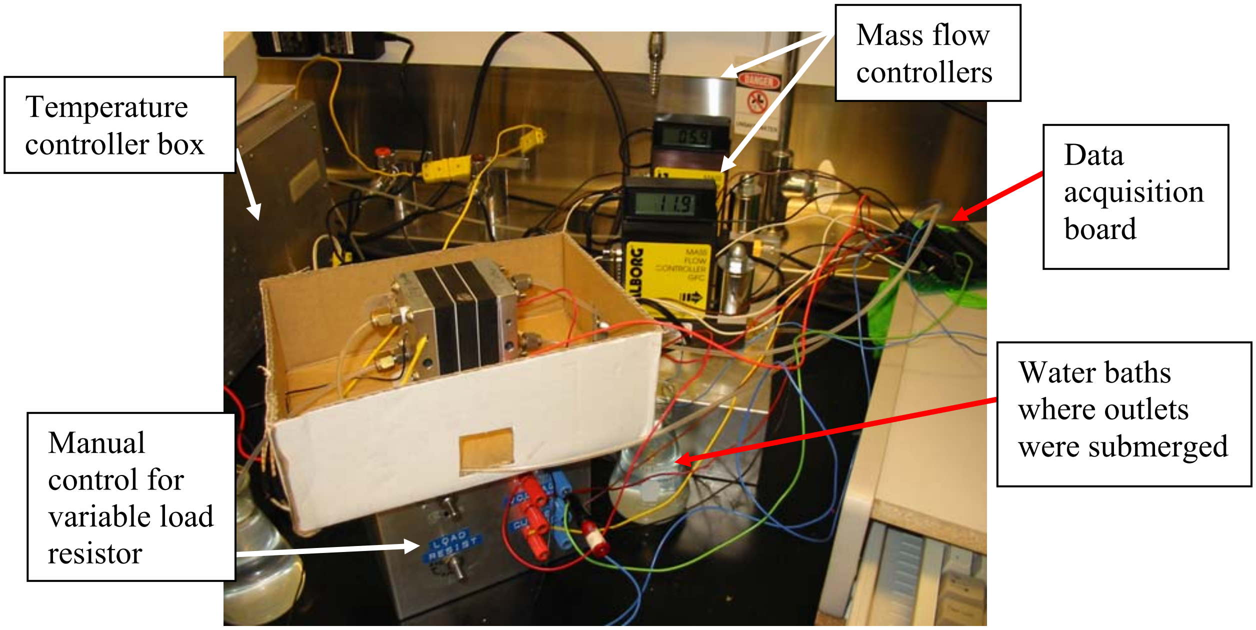

Figure 3.7 Complete Experimental Setup with fuel cell stack connected to gas flow controllers, load resistor, and temperature controller.

Figure 3.7 shows the complete experimental setup, including the fuel cell stack, gas flow controllers, load resistor, connections to the DAC board, and gas flow connections. For all tests, the two-cell stack was first equilibrated at 60^{o}C, a load resistance of 2Ω, and constant H_2/O_2 flow rates prior to sweeping IV curves. The three-cell stack was equilibrated at 3Ω before the IV sweep. Typically, it took between 1 to 4 hours for the stack to reach steady-state. After steady-state was reached, an IV curve was obtained by manually varying the external load resistance from 110Ω to 0.46Ω within 100 seconds while measuring the corresponding current and voltage. For all tests conducted, no humidification of feeds or manual injection of liquid water was necessary for ignition or for continuous operation of the fuel cell stack.

4. Results and Discussion

Results from two-cell stack testing are first presented, followed by results of three-cell stack testing. Both transient and steady-state performances were examined. IV curves were also used to compare performances at various operating conditions. As mentioned in Section 3.3, due to variations in the quality of individually-pressed MEAs, comparison of absolute values between different sets of data was difficult. Instead, general behavioral trends were identified. Next, long-term stability of the three-cell stack was examined. Water production and removal during long-term operation was briefly discussed. Then results of current control by fuel starvation were presented. Lastly, the results of the stainless steel stack were compared with that of the graphite stack, followed by a critique of the suitability of each material.

4.1 Two-Cell Stack Dynamics

4.1.1 Stoichiometric Feeds

The two-cell stack was first operated at stoichiometric H_2/O_2 flow rates (i.e. H_2 to O_2 feed ratio is 2). Table 4.1 shows the steady-state current and voltages at 60^oC and 2Ω load. For 10/5 mL/min flow and above, there were no significant variations in overall performance. Bubbles were observed to exit continuously at both the cathode and anode outlet, which confirmed that reactants were always in excess. IV curves obtained are shown in Figure 4.1. Internal resistances R_{int} were calculated from the negative slope of the ohmic region of the IV curves and were also recorded in Table 4.1.

Interestingly, 14/7 and 12/6 mL/min feed flows produced the largest output power during steady-state as well as during IV sweeps. At 14/7 and 12/6 flows, R_{int} matched the external load R_L, which coincided with the claims by Benziger et al. [24] that maximum

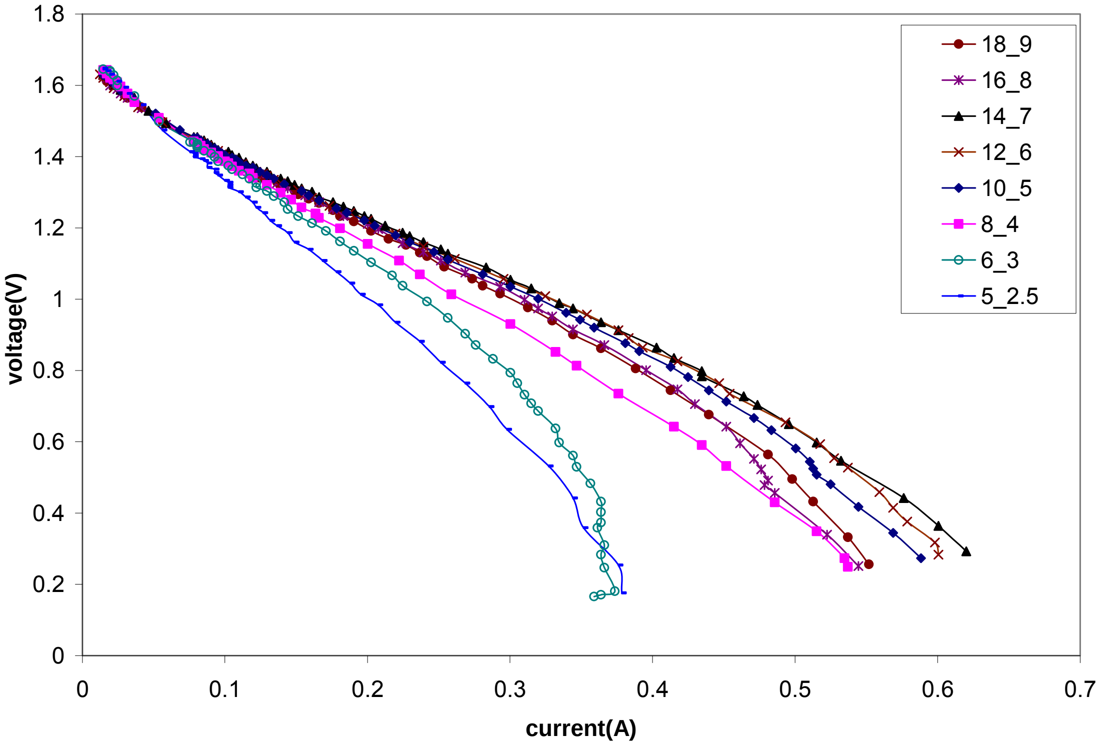

Figure 4.1 IV curves obtained at various H_2/O_2 flow rates [mL/min] after the fuel cell stack had been equilibrated at 2Ω and 60°C for more than 3 hours and steady state was achieved. At flow rates of 10/5 and above, results were similar, and gas bubbles were consistently observed at both H_2 and O_2 outlet, indicating that reactants were in excess. 14/7 and 12/6 flow conditions exhibited the largest output power, which could be due to the matching of the internal impedance R_{int} and the load impedance R_L. Starvation condition was believed to be attained at flow rates of 8/4 and below when bubbles were only intermittently observed at the outlets.

H_2/O_2 flow [mL/min]	Current [A]	V_{total} [V]	V_A [V]	V_B [V]	$\lvert V_A-V_B\rvert$ [V]	R_{int} [Ω]	$R_{int,A}$ [Ω]	$R_{int,B}$ [Ω]	Power [W]
18/9	0.37	0.73	0.37	0.36	0.01	2.52	1.44	1.09	0.270
16/8	0.37	0.75	0.39	0.36	0.03	2.67	1.49	1.18	0.278
14/7	0.40	0.79	0.41	0.38	0.04	2.12	1.18	0.95	0.316
12/6	0.39	0.78	0.42	0.37	0.05	2.07	1.07	0.98	0.304
10/5	0.38	0.76	0.38	0.38	0	2.28	1.22	1.05	0.289
8/4	0.31	0.62	0.25	0.37	0.12	2.57	1.33	1.25	0.192
6/3	0.22	0.44	-0.04	0.48	0.52	4.73	2.87	1.91	0.097
5/2.5	0.18	0.36	-0.08	0.44	0.52	4.19	2.37	1.79	0.065

Table 4.1 Steady-state current, voltage, internal resistances, and output power of 2-cell stack equilibrated for more than 3 hours at 60°C and 2Ω at various stoichiometric feed flow rates. Maximum power was obtained at 14/7 and 12/6 flow when internal resistance and load resistance matched ($R_{int} = R_L = 2Ω$). R_{int} increased significantly at lower flow rates due to flooding as water was pushed into the stack by the larger external pressure.

power could be achieved by matching these two impedances. As shown in Table 4.2, the excess ratio λ (= reactant fed/ reacted) also happened to be closest to 2 for these two flow conditions. The excess ratio λ of 2 had been suggested by several authors [4-6] as the magic ratio for optimal performance. This claim was born out of water management considerations. If flow is too high, water is pushed out of the fuel cell faster than it is generated, which leads to drying of the membrane. Reduced water activity decreases proton conductivity. On the other hand, if flow is too low, water starts to accumulate in the gas flow channels, leading to flooding, which reduces the active membrane area and also affects cell performance.

H_2/O_2 flow [mL/min]	H_2 fed [mmol/min]	H_2 used in 2 cells [mmol/min]	H_2 utilization [%]	excess ratio λ = fed/reacted
18/9	0.73	0.23	32	3.16
16/8	0.65	0.23	36	2.81
14/7	0.57	0.25	44	2.27
12/6	0.48	0.24	50	2.00
10/5	0.40	0.24	59	1.71
8/4	0.32	0.19	60	1.68
6/3	0.24	0.14	56	1.77
5/2.5	0.20	0.11	55	1.80

Table 4.2 H_2 utilization and excess ratio λ calculated for the test results at various stoichiometric flows. Calculations were based on a H_2 mole balance. At 14/7 and 12/6 flow, where maximum power was generated (Table 4.1), λ was 2, which coincided with the value suggested by most literature as the magic ratio for optimized performance due to water management considerations.

Water activity also depends on the stack operating temperature because of the dependence of water vapor pressure $P_{vp,w}$ on temperature. For example, $P_{vp,w}$ increases from 0.03 bar at 25°C to 0.2 bar at 60°C and to 1.0 bar at 100°C. Thus, in non-pressurized conditions, almost all the water formed by the reaction will condense at 25°C, whereas almost all the water will be able to stay in vapor phase at 100°C. For a commercial fuel cell operating at 60°C, an excess ratio of 2 has been calculated to be high enough flow to keep liquid water out and also low enough to not dry out the membrane by convective gas flow [8].

Since relative humidify sensors were not put into the system, it was difficult to determine whether the membrane was dry or wet under different flow conditions studied. However, a simple water balance could be performed to look at possible scenarios. In the flow field design of the stack, as shown in Figure 3.6, H_2 and O_2 feeds each had one inlet. Ideally, half of the gas would go to cell A, and the other half would go to cell B to ensure equal performance. But there was no guarantee that reactant distribution was uniform. In fact, differences in cell voltages and internal resistances indicated that uniform distribution was rarely achieved. Cell A probably received more H_2 whereas cell B likely received more O_2.

Table 4.3 shows the water balance for cell A at different ratios of reactant distribution at 18/10 mL/min flow condition. Steady-state current attained was 0.37A, which meant that 0.115 mmol/min H_2 and 0.0575 mmol/min O_2 were consumed. In the first case, 80% of the H_2 feed (0.58mmol/min) and 50% of the O_2 feed (0.18mmol/min) went to cell A. By mole balance, 0.46mmol/min H_2 and 0.12mmol/min O_2 should exit cell A. Assuming that the anode and cathode had similar P_w and that steady-state was reached (i.e. no water accumulation in membrane, so), theoretical P_w in cell A could be determined from Equation 4.1, which was simplified from Equation 2.8. Assuming that all the water produced by the reaction was removed by convection from anode and cathode, partial pressure of water would be 0.19bar, which was slightly smaller than the vapor pressure of water at 60°C. Thus it is possible that membrane was slightly dehydrated at this flow distribution.

$$P_w = \frac{i}{2F} * \left(\frac{RT}{Q_A^{out} + Q_C^{out}}\right) \tag{4.1}$$

Reactant distribution		H_2 in [mmol/min]	O_2 in [mmol/min]	H_2 out [mmol/min]	O_2 out [mmol/min]	P_w [bar]
H_2	O_2					
80%	50%	0.58	0.18	0.47	0.12	0.19
80%	20%	0.58	0.073	0.47	0.015	0.24
70%	30%	0.51	0.11	0.39	0.052	0.26
60%	40%	0.44	0.15	0.32	0.089	0.28
50%	50%	0.36	0.18	0.25	0.12	0.31

Table 4.3 Water balance for cell A at different reactant distribution ratio for 18/10 flow. For example, in the highlighted row, 80% of H_2 and 50% of O_2 supplied to the stack was assumed to be distributed to cell A. For 18/9 flow, it meant 14.4mL of H_2 and 4.5mL of O_2 went to cell A. P_w was calculated from the assumption that all the water produced stayed in vapor phase. Steady-state current was 0.37A, so rate of water production was 0.12mmol/min. As expected, if more H_2 passes through cell A, the possibility of drying increases, as indicated by the first case of 80/50% distribution where $P_w < P_{vp} = 0.2$bar. It can be inferred that membrane drying was likely to occur at even higher H_2 flow rates.

As mentioned in Section 2.4, membrane hydration is desired in order to give maximum proton conductivity. Table 4.3 shows that if reactants were more evenly distributed, the likelihood of membrane drying decreased. At lower flow rates, less gas would flow through the stack and P_w should theoretically be even higher. Thus, for most of the flow rates used, membrane drying was probably not a problem.

On the other hand, the fact that P_w was larger than $P_{vp,w}$ suggested that the vapor phase was oversaturated and at least some of the water generated should have condensed in the stack. Ideally, the self-draining ability of the STR fuel cell stack should have removed the liquid water and prevented flooding. Figure 4.2 shows a picture of liquid water being pushed out of the oxygen flow channels through the O_2 outlet tube.

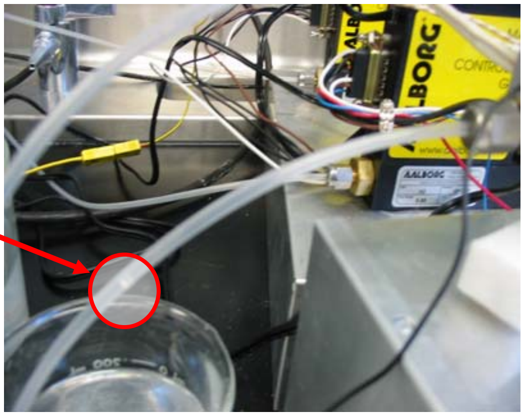

Figure 4.2 Liquid water is pushed out of the O_2 flow channels through the O_2 outlet during a test.

Unfortunately, calculations of internal resistances suggested that liquid water removal was not perfect in the stack, especially at lower flow rates. For 10/5 flow and below, R_{int} increased dramatically. The increase was coupled with the observation that gas bubbles were no longer continuously seen at the outlets. Instead, water in the water bath was often seen to be sucked into the cell. This was because at lower flows, a vacuum was created near the outlet, and the larger atmospheric pressure pushed water into the stack. Water buildup reduced active membrane area, causing an increase in R_{int}.

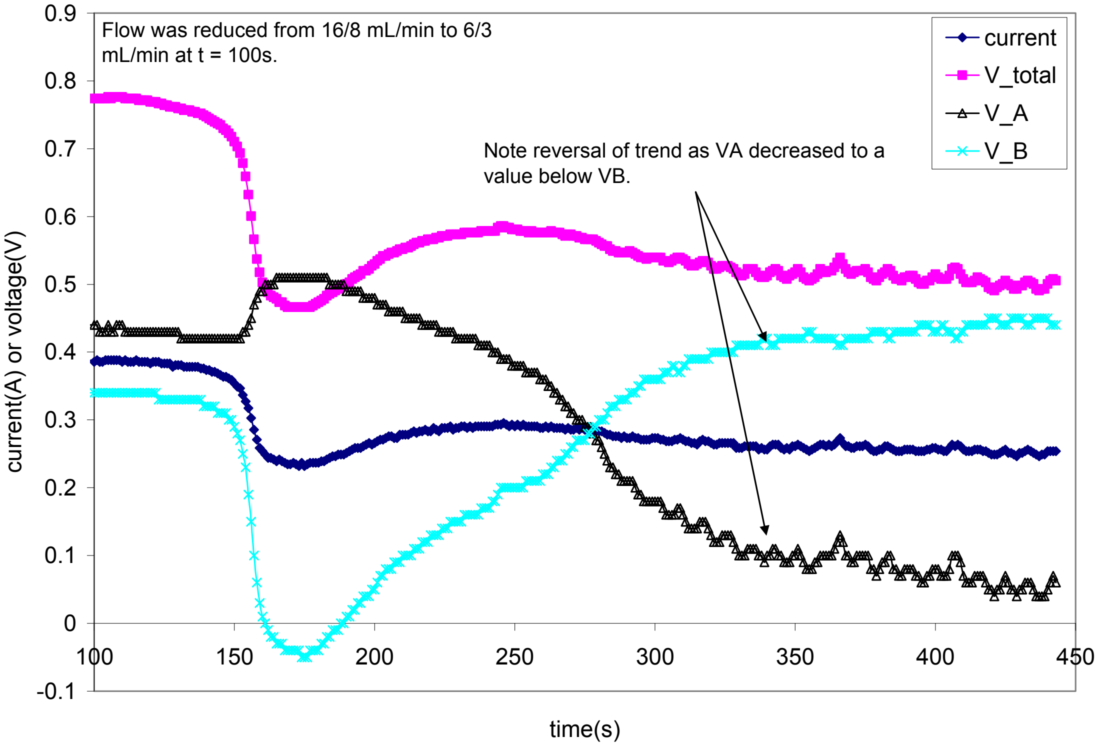

Figure 4.3 Transient stack response when H_2/O_2 flow rates were reduced from 16/8 to 6/3 mL/min at t = 100s. V_A decreased to a value below V_B within 200s. The lag in time response was due to excess reactants stored in gas flow channels, which was able to sustain a higher current for awhile. The decrease of V_A after flow rates were reduced was due to a combination of O_2 starvation and flooding in cell A.

Besides flooding, other things were happening at lower flow rates. V_A and V_B values were comparable until H_2/O_2 flow rates were reduced to below 10/5 mL/min. V_A even became negative at 6/3 and 5/2.5 mL/min flows, meaning that cell A became electrolytic. Figure 4.3 shows that V_A, which was slightly higher than V_B at 16/8 mL/min flow, decreased dramatically after the flow was reduced to 6/3 mL/min at t = 100s. There were 2 possible reasons for this. One was the aforementioned problem of flooding. There could have been more flooding in cell A cathode because of less O_2 flowing through cell A. This coincided with the larger $R_{int,A}$ at lower flows. According to Equation 2.3, a larger $R_{int,A}$ would led to decrease in V_A. Flooding was probably more severe in cell A than in cell B since water was generated in the cathode and because total O_2 flow was half of H_2 flow.

The second reason for the reduced performance of cell A was mass transfer limitations of O_2 to the catalyst surface of the cathode in cell A. Since O_2 was fed into cell B first, cell A probably received less O_2 and thus was affected more by O_2 mass transfer limitations. O_2 has a mass transfer coefficient of 0.35 amp/bar, whereas H_2 has a mass transfer coefficient of 1.0 amp/bar. Because of slower diffusivity of O_2, mass transfer limitation of O_2 affected cell A well before mass transfer limitation of H_2 was reached in cell B. Thus, the decrease in cell A performance was probably due to a combination of flooding and mass transfer limitations of O_2.

In addition, cell reversal (i.e. cell A becoming electrolytic) at these low flow rates could cause long-term damage to the Pt catalyst [27]. These results suggested that problems such as flooding and uneven distribution of reactants would arise during fuel starvation. Moreover, control by fuel starvation is anticipated to fail unless performance of individual cell performance is sacrificed.

One interesting observation should be made about the IV curves shown in Figure 4.1. The IV curves were obtained by quickly varying the external load from 110Ω to

0.46Ω within 100s. This was to ensure that water activity in membrane remained the same for the duration of the sweep. At 8/4 mL/min flow, assuming that there was no mass transfer limitation, if H_2 and O_2 were evenly distributed between the individual cells and were completely used up, a maximum current of 0.52A could theoretically be generated. Surprisingly, the highest current obtained during the fast IV sweep was even larger than this theoretical limit.

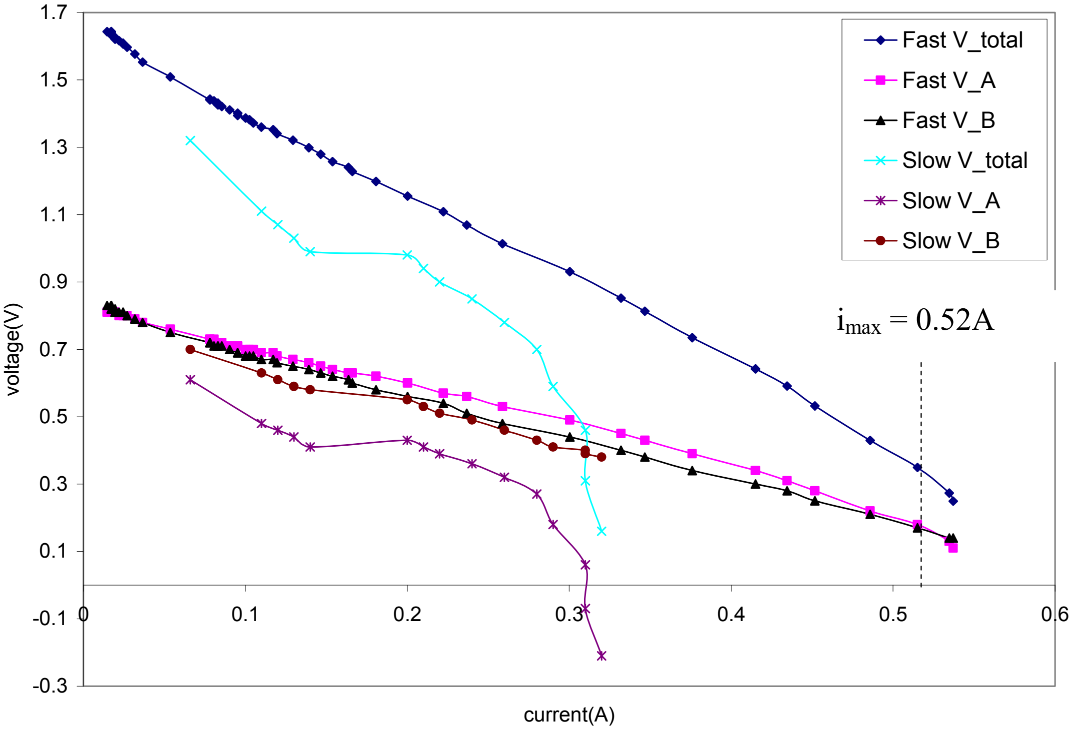

Figure 4.4 Comparison of a fast IV sweep and a steady-state (slow) IV curve at 8/4 mL/min H_2/O_2 flow. Maximum current obtained during the fast IV sweep was slightly larger than theoretically possible limit. There must have been a net depletion of reactant in the STR fuel cell. In contrast, the slow IV curve was obtained by ensuring that the fuel cell reached steady-state at each load resistance applied. The difference between V_A and V_B was larger in the steady-state IV curve. Also, O_2 mass transfer limitation in cell A was more evident when the stack was allowed to reach steady-state. The discrepancy in the results of fast and slow IV curves questions the validity of using a fast IV sweep as a means for cell performance evaluation.

Figure 4.4 illustrates this point more clearly by showing the IV curve and maximum theoretical current for 8/4 mL/min flow. At current higher than 0.52A, since more current was being generated than supplied, there must have been a net depletion of reactants in the gas flow channels. This effect was possible because extra reactants were stored in the gas flow channels. In essence, this reactant reservoir added a capacitance element to the fuel cell. The volume of anode was about $0.66 cm^3$. If 50% H_2 went to cell A, the residence time of H_2 in the anode was about 10s (= V_{anode}/Q_H). This represents the equivalent RC time constant for the fuel cell. Since the stack was not pressurized, at 60°C, a maximum of 2.38e-5 mol of H_2 could be stored in the gas flow channels, which could generate 4.6 coulombs of charge.

From the RC time constant calculated, one could predict that current could not be sustained at >0.52A for longer than 10s. In fact, this was exactly what was observed when the stack was allowed to reach steady-state at each load resistance, generating a steady-state IV curve. Figure 4.4 shows the comparison between a fast IV sweep and a steady-state IV curve. Maximum current obtained in the steady-state IV curve was 0.32A, well below the theoretical maximum value of 0.52A. The fuel cell stack showed elevated performance during the fast IV sweep (i.e. at constant water activity and membrane hydration). This was probably a result of the capacitance of the fuel cell. Reactants stored in the gas flow channels slowed down the dynamic response of the fuel cell to load changes. Thus, the result of the steady-state IV curve was more reliable as it illustrates the performance of the fuel cell for a longer duration. The difference between V_A and V_B was also larger in the steady-state IV curve. As explained before, this could have been due to more serious flooding in cell A cathode, which was receiving less O_2 than cell B. The discrepancy in the results of a fast IV curve and a steady-state IV curve leads one to question the validity of using a fast IV sweep as a means for fuel cell performance evaluation.

4.1.2 Effect of Varying Hydrogen Flow Rate

Figure 4.5 shows the IV curves obtained at various H_2 flow rates while O_2 flow was kept constant at 8mL/min. Performance steadily decreased as H_2 flow was decreased. When H_2 flow was reduced to 8mL/min and below, bubbles stopped exiting the outlets at high current (low load), indicating that starvation condition was reached. At 8/8 flow, the steadily increasing current experienced a reversal at low loads where it suddenly decreased. Similar results were obtained in the three-cell stack and are explained in further details in Section 4.2.

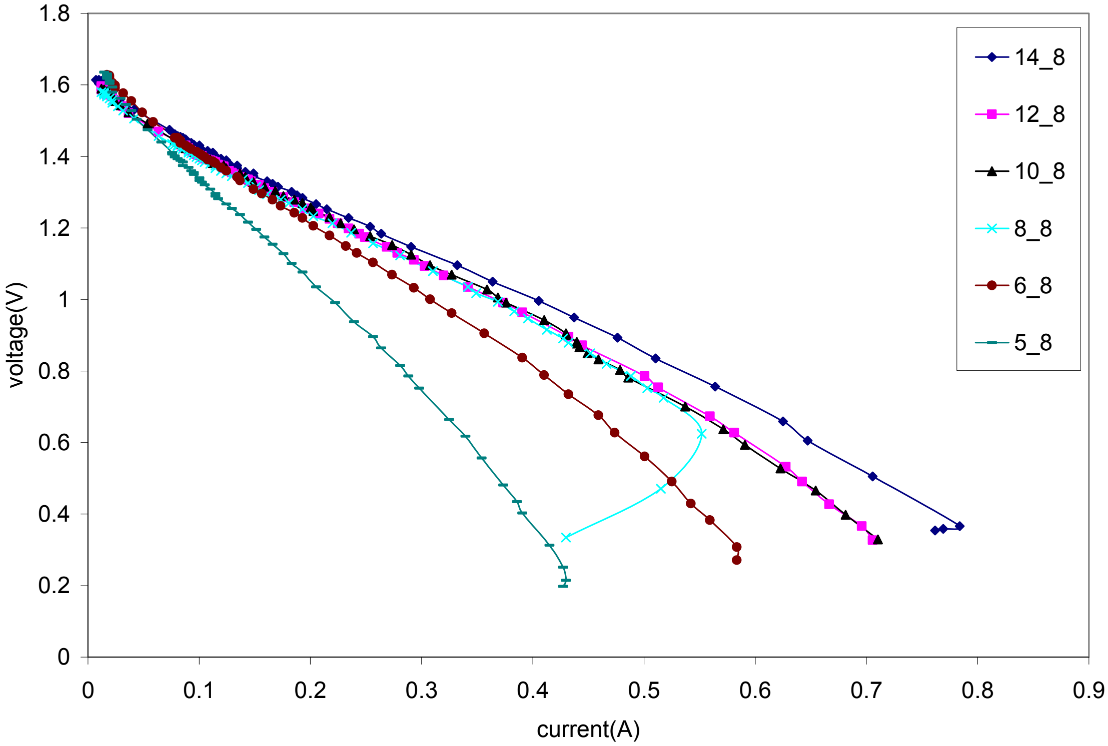

Figure 4.5 IV curves at various H_2 flow rates while keeping O_2 flow constant at 8mL/min. Curves were obtained after more than 3 hours of equilibration at 2Ω and 60°C. Performance steadily decreased as H_2 flow was decreased. When H_2 flow was reduced to 8mL/min and below, bubbles stopped exiting the outlets at high current (low load), indicating that starvation condition was reached.

Table 4.4 summarizes the steady-state current, voltages and internal resistances. Steady-state performance at 10/8 mL/min flow and above was comparable, outputting a current of 0.42A at 2Ω load. As H_2 flow was reduced, current decreased and R_{int} increased. In addition, there was a growing disparity between individual cell voltages at reduced flows. In contrast to stoichiometric flows where V_A decreased at lower flow rates, V_B decreased significantly when only H_2 flow was reduced.

H_2/ O_2 flow [mL/min]	Current [A]	V_{total} [V]	V_A [A]	V_B [B]	$\|V_A-V_B\|$ [V]	R_{int} [Ω]	$R_{int,A}$ [Ω]	$R_{int,B}$ [Ω]	Power [W]
14/8	0.42	0.84	0.46	0.37	0.09	1.51	0.61	0.92	0.353
12/8	0.42	0.84	0.47	0.37	0.10	1.65	0.66	0.98	0.353
10/8	0.42	0.84	0.47	0.37	0.10	1.72	0.68	1.05	0.353
8/8	0.38	0.76	0.5	0.26	0.24	1.78	0.79	0.98	0.289
6/8	0.29	0.58	0.5	0.08	0.42	2.24	0.99	1.23	0.168
5/8	0.20	0.4	0.48	-0.06	0.54	3.4	1.83	1.56	0.080

Table 4.4 Steady-state current, voltage, internal resistances, and output power of 2-cell stack equilibrated for more than 3 hours at 60°C and 2Ω at various H_2 flow rates while O_2 flow was kept constant at 8mL/min. Current and power dropped at 6/8 flow as R_{int} increased dramatically due to flooding and H_2 starvation in cell B.

Since cell B was downstream of cell A for H_2 flow, starvation of H_2 was expected to affect cell B more, limiting V_B to smaller values. As bubbles stopped exiting the H_2 outlets, liquid water was no longer removed by gas convection, thus leading to flooding in the anode chamber, especially in cell B. This was confirmed by the increase in $R_{int,B}$ at low H_2 feed, as illustrated in Table 4.4. Thus, a combination of flooding and H_2 starvation resulted in lower cell B performance.

In addition, Figure 4.6 shows that current became unstable at lower H_2 flow rates. These types of instabilities were not observed during starvation of the single STR fuel cell. One of the unique features of the STR fuel cell was the lack of horizontal surfaces in the flow channels. However, in the fuel cell stack, horizontal surfaces were introduced in the channels connecting individual cells. Figure 4.7 illustrates the imperfect draining system in the fuel cell stack. Accumulation of water in the horizontal middle channels could have caused instabilities in stack performance. These instabilities would create problems when control by fuel starvation was attempted later. However, this hypothesis needs to be quantified. Future work should be done on measuring and/or monitoring water level inside the stack. Furthermore, stack design can be improved by making the connecting channels slanted in order to get rid of horizontal surfaces and facilitate better drainage.

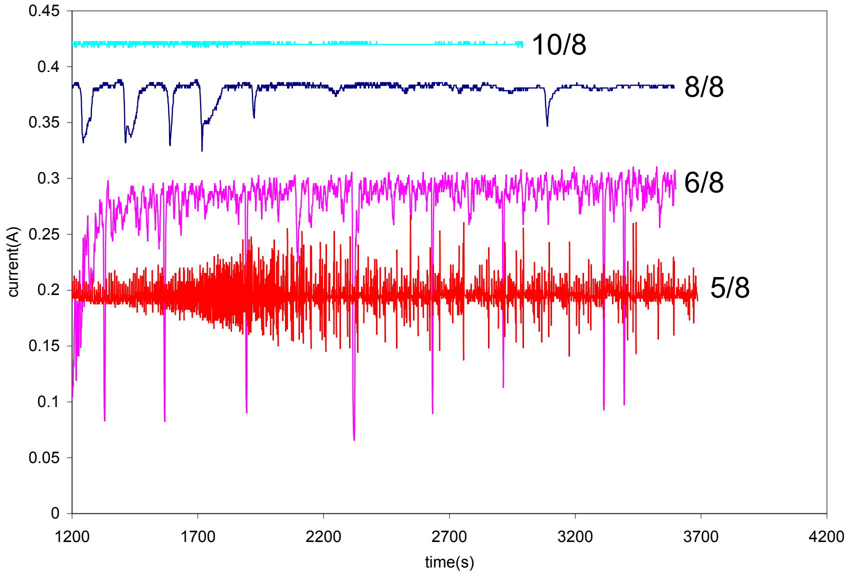

Figure 4.6 Transient current at different H_2/O_2 flow rates [mL/min]. As H_2 flow is reduced, especially at 6mL/min and 5mL/min, current becomes unstable. Instability could be caused by a combination of water buildup in connecting channels and reactant starvation in cell B.

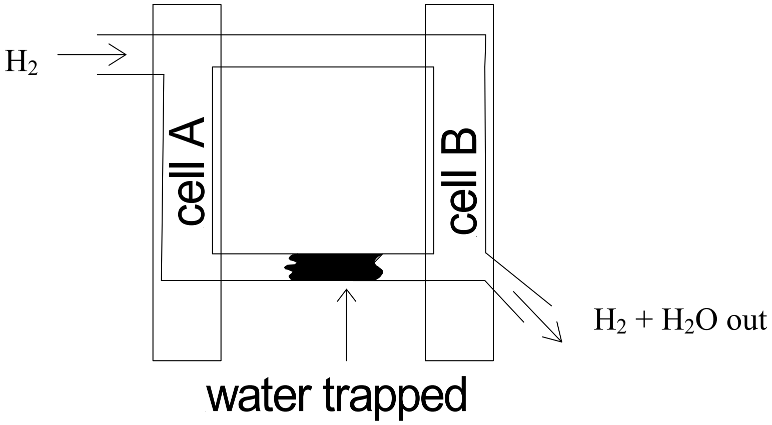

Figure 4.7 Imperfect draining system in STR fuel cell stack. The stack design introduced horizontal surfaces, and liquid water could potentially be trapped in channels connecting the two individual cells.

Figure 4.8 shows the transient response of the fuel cell stack at H_2 starvation condition. At 14/8 flow, V_A and V_B were similar in value. At t = 500s, H_2 flow was reduced from 14 to 6mL/min. Within 30 seconds, current dropped from 0.4A to 0.03A. Bubbles stopped exiting the H_2 outlet, and cell A quickly became electrolytic whereas V_B increased. At the same time, water was observed to enter the stack from the water bath at the H_2 outlet. As H_2 flow was reduced, there was a net depletion of H_2 in the stack, so pressure in the anode decreased, creating a small vacuum at the outlet, which then allowed the larger atmospheric pressure outside to push water into the cell.

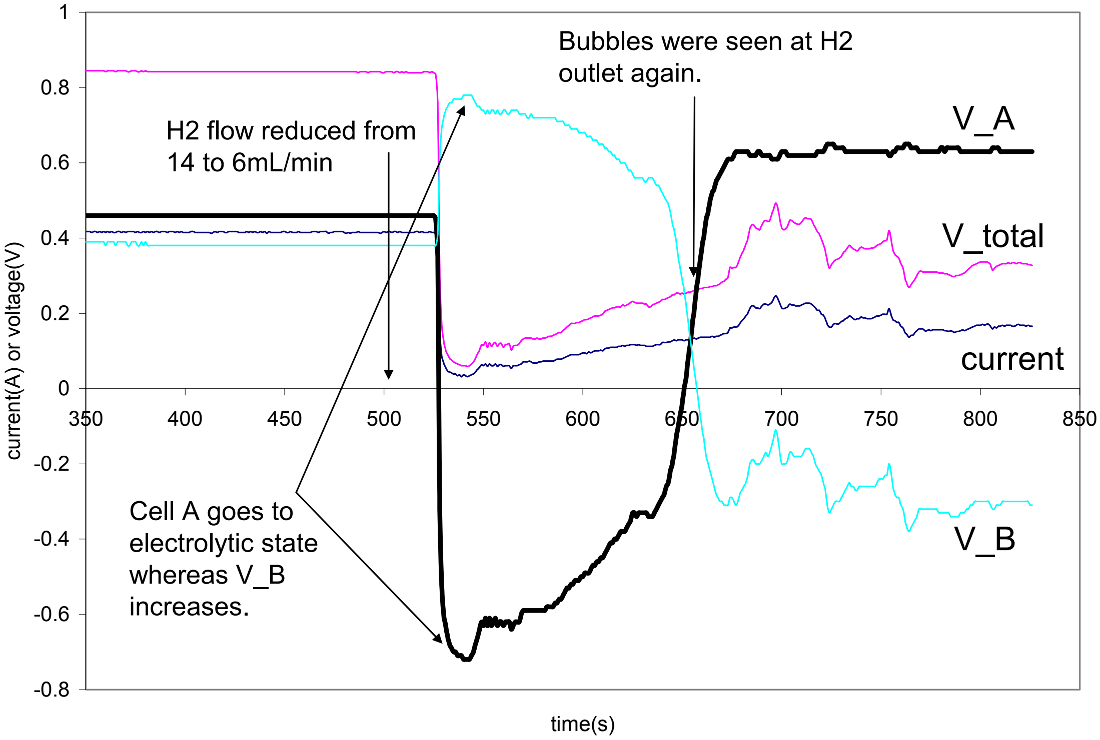

Figure 4.8 Transient response of fuel cell stack when H_2 flow rate was reduced from 14 to 6mL/min at t=500s while O_2 flow was kept constant at 8mL/min. At 14/8 flow, V_A and V_B were similar. When flow was reduced, current dropped within 30 seconds. At the same time, bubbles stopped exiting the H_2 outlet and water from the water bath at the H_2 outlet was pushed into the stack by the larger atmospheric pressure outside. Flooding of cell A probably caused the reversal of cell A to electrolytic state. Then at t=650s, bubbles were seen again at the H_2 outlet at the same time that V_A recovered. In other words, as water was pushed out of the stack, cell A recovered.

Water that entered the stack could have flooded cell A or cell B. In this case, it probably flooded cell A since cell A became electrolytic. Then, at t ≈ 650s, bubbles were observed at H_2 outlet again. At the same time, V_A increased to 0.6A while V_B became electrolytic. This observation suggested that water accumulated was pushed out of the stack and cell A recovered from flooding. At the same time, V_B became electrolytic as cell A was using up most of the H_2 supplied, and cell B went into starvation condition.

4.1.3 Effect of Varying Oxygen Flow Rate

Next, the effect of varying O_2 flow was examined. Table 4.5 summarizes the stack performance at 3 different O_2 flow rates while H_2 flow was kept constant at 16mL/min. In contrast to H_2 starvation where V_B decreased to lower values, cell A performance was more affected at O_2 starvation. Stack performance started to decrease when O_2 flow rate was reduced to 4mL/min. IV sweep was not successful at this flow because of two reasons. One, the stack was unstable at this flow condition and current never reached steady-state. Second, the stack would extinguish at small loads (i.e. high current). Thus, exact internal resistances of the cells could not be calculated for 16/4 flow, but they were probably higher than R_{int} at high O_2 flows.

H_2/ O_2 flow [mL/min]	Current [A]	V_{total} [V]	V_A [A]	V_B [B]	$\lvert V_A-V_B \rvert$ [V]	R_{int} [Ω]	$R_{int,A}$ [Ω]	$R_{int,B}$ [Ω]
16/5	0.39	0.79	0.45	0.34	0.11	2.03	0.89	1.13
16/4.5	0.39	0.77	0.39	0.38	0.01	2.23	1.25	0.96
16/4	0.30-0.32	0.60-0.63	0.12-0.15	0.48-0.49	0.35	-	-	-

Table 4.5 Current, voltage, internal resistances, and output power of 2-cell stack equilibrated for more than 3 hours at 60°C and 2Ω at various O_2 flow rates while H_2 flow was kept constant at 16mL/min. Current and power dropped at 16/4 ml/min flow as cell A was starved of O_2. Steady-state was never reached at this flow rate.

Figure 4.9 shows the transient performance of the stack when O_2 flow rate was reduced from 8 to 4mL/min at t = 200s while H_2 flow was kept constant at 16mL/min. At 16/8 flow, V_A and V_B values were close. When O_2 flow was reduced by half, current maintained itself at 0.4A for 200s until at t ≈ 400s it dropped to about 0.3A. The drop in current coincided with the discontinuation of gas bubbles exiting the O_2 outlet. V_A decreased quickly whereas V_B increased. Less O_2 was probably reaching cell A, which was downstream of cell B in terms of O_2 flow, thus limiting V_A to a smaller value. More importantly, the lack of gas bubbles at O_2 outlet meant that pressure in the cathode chamber of cell A was lower than atmospheric pressure, and water was again observed to be sucked into the cell, causing flooding and consequently a decrease in active membrane area in cell A.

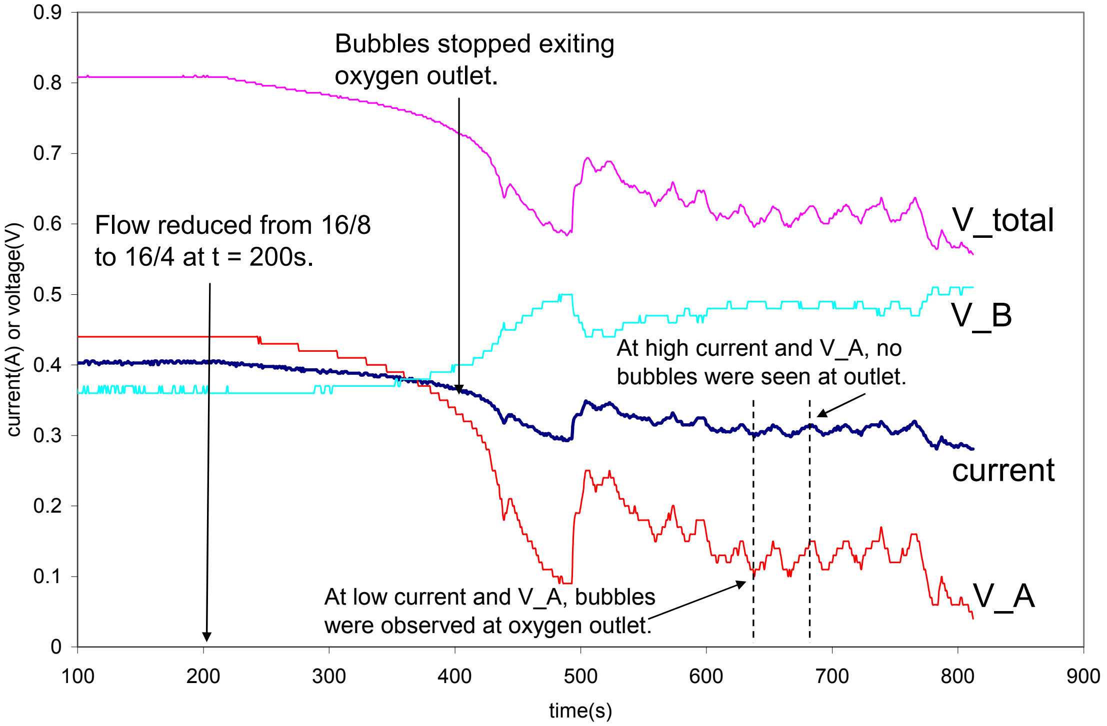

Figure 4.9 Transient response of fuel cell stack when O_2 flow rate was reduced from 8 to 4mL/min at t=200s while H_2 flow was kept constant at 16mL/min. At 16/8 flow, V_A and V_B were similar. When O_2 flow was reduced, current was able to stay at previous level until t ≈ 400s when bubbles stopped coming out of O_2 outlet, which was indicative of starvation condition. V_A quickly dropped whereas V_B increased. Between t=600s and 800s, small in-phase oscillations of current and voltage were observed as gas bubbles were intermittently seen at the O_2 outlet. Oscillations were the result of cell A going between a flooded state and a non-flooded state.

Interestingly, oscillatory behavior was observed between t = 600s and t = 800s. The oscillations in current and voltage were in-phase. V_A oscillated a lot more than V_B.

These oscillations were coupled with the observation of bubbles being intermittently seen at the O_2 outlet. When no bubbles were exiting, current gradually decreased until bubbles were seen at O_2 outlet again, then current would increase. As current started increasing, bubbles stopped exiting again. In other words, bubbles were only observed for a brief moment at low current values, as indicated in Figure 4.9.

At low current, less O_2 was being consumed, so exit flow was slightly higher. This helped push a little bit of water out of cell A, freeing up some active membrane area and thus allowing current to increase. However, as current increased, exit O_2 flow became lower, which allowed water to enter cell A again, thus blocking parts of the MEA. So current decreased again. In other words, the oscillations were probably due to slight changes in water level inside cell A. A similar mechanism might be happening in cell B as well since V_B was also oscillating, though at a smaller amplitude.

In summary, test results of the two-cell stack at different flow conditions demonstrated that flooding and starvation could cause instability at low flow rates. These were expected to cause problems later in current control by fuel starvation. Defects in the drainage system of the stack were hypothesized to be an important factor affecting the stack performance. In addition, uneven distribution of reactants led to reduced performance in one cell. If one cell reached starvation, it would limit the current that could be produced by the stack. Thus, for better performance, uniform reactant distribution was recommended. This could be achieved by modifying the gas feed manifolds and flow pattern in the STR fuel cell stack.

4.2. Three-Cell Stack Dynamics

A cell was added to the two-cell stack to make a three-cell stack, and stack performance at various flow conditions were examined. Table 4.6 shows the steady-state results of the stack at different H_2 flow rates, including the current, voltages, and internal resistances calculated from the negative slope of the ohmic region in the IV curve. As a general trend, current and V_{total} decreased with H_2 flow rate whereas R_{int} increased as H_2 flow was reduced. This was likely due to water accumulation in cell B and cell C, as suggested by the increase in their internal resistances.

H_2/O_2 flow [mL/min]	Current [A]	V_{total} [V]	V_A [V]	V_B [V]	V_C [V]	$R_{int,total}$ [Ω]	$R_{int,A}$ [Ω]	$R_{int,B}$ [Ω]	$R_{int,C}$ [Ω]
22/10	0.53	1.59	0.54	0.48	0.56	1.09	0.30	0.45	0.36
20/10	0.53	1.64	0.56	0.52	0.56	1.16	0.34	0.46	0.37
18/10	0.53	1.62	0.56	0.51	0.55	1.17	0.36	0.46	0.38
16/10	0.52	1.54	0.58	0.42	0.55	1.30	0.36	0.44	0.50
14/10	0.50	1.50	0.56	0.45	0.49	1.46	0.44	0.58	0.44
12/10	0.43	1.30	0.61	0.55	0.13	1.59	0.37	0.66	0.59
10/10	0.41	1.23	0.61	0.38	0.24	1.74	0.43	0.73	0.58

Table 4.6 Steady-state current, voltages and internal resistances of stack and individual cells at different H_2/O_2 flow rates at 60°C. V_B was consistently lower than V_A and V_C for H_2 flow of 14mL/min and above. At 12 and 10 mL/min H_2 flow, V_C decreased to relatively smaller values, indicating that cell C was probably starved of H_2 at this flow. R_{int} also showed a steadily increasing trend with decreasing flow rates, which is expected due to increasing chances of flooding at lower flow conditions.

At lower H_2 flows of 10 and 12mL/min, V_A was highest and V_C was lowest. This steadily decreasing trend was to be expected according to the position of each cell along the H_2 flow channel. More H_2 was probably distributed to the upstream cell A than the downstream cell B and cell C, thus leading to a steadily decreasing cell voltage along the stack. At these flow rates, gas bubbles also stopped exiting the H_2 outlet, suggesting that cell C and possibly cell B were starved of fuel, which was confirmed by the low V_C.

On the other hand, at H_2 flow of 14mL/min and above, V_B was consistently lower than both V_A and V_C. The internal resistance of cell B was also slightly higher than that of cell A and cell C for all flow conditions. One possible explanation for this anomaly was the trapping of water in channels on both sides of cell B. Cell B is located in the middle of the stack where it is not connected to any downward-sloping channels to allow for gravity-driven water drainage. Thus, water could easily be trapped in channels flanking both sides of cell B. As water accumulated over time, it reduced the active area of the cell B MEA, thus leading to a larger $R_{int,B}$ as well as a lower V_B.

Table 4.7 shows the H_2 utilization rate at different flow conditions. At 10mL/min H_2 flow rate, as high as 95% H_2 utilization was achieved. Unfortunately, current and cell voltages also became less stable at such low flow rates, as shown in Figure 4.10. This observation coincided with results of the 2-cell stack where current became unstable when one cell in the stack was starved. Instability was probably due to water accumulation, which directly affected the active membrane area and internal resistances.

H_2/O_2 flow [mL/min]	H_2 feed [mol/min]	Current [A]	H_2 used in 1 cell [mol/min]	H_2 used in 3 cells [mol/min]	H_2 utilization rate [%]
22/10	8.88e-04	0.53	1.65e-04	4.94e-04	56
20/10	8.07e-04	0.53	1.65e-04	4.94e-04	61
18/10	7.27e-04	0.53	1.65e-04	4.94e-04	68
16/10	6.46e-04	0.52	1.62e-04	4.85e-04	75
14/10	5.65e-04	0.5	1.55e-04	4.66e-04	83
12/10	4.84e-04	0.43	1.34e-04	4.01e-04	83
10/10	4.04e-04	0.41	1.27e-04	3.82e-04	95

Table 4.7 H_2 utilization rate (=fed/reacted*100%) at different flow conditions. At 10mL/min H_2 flow rate, as high as 95% H_2 utilization was achieved. However, stack performance in terms of current output was also less stable at this flow (see Figure 4.10).

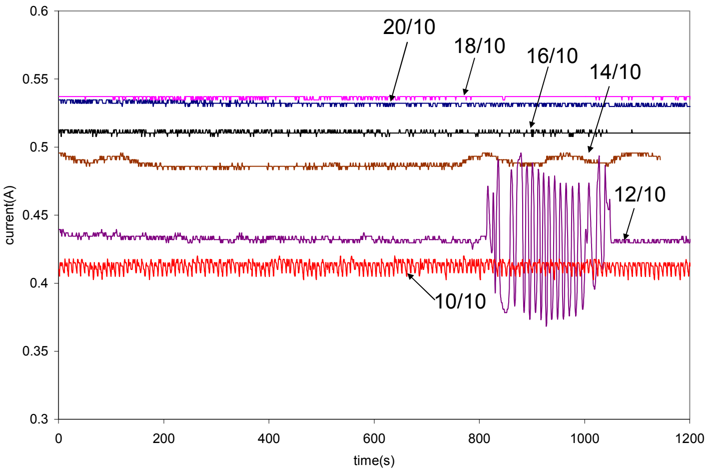

Figure 4.10 Transient current of 3-cell stack at 60oC and 3 Ω at different H_2/O_2 flow rates as indicated on the graph. Current became less stable at lower H_2 flow rates possibly due to water plugs in the channels. Corresponding cell voltages are indicated in Table 4.6.

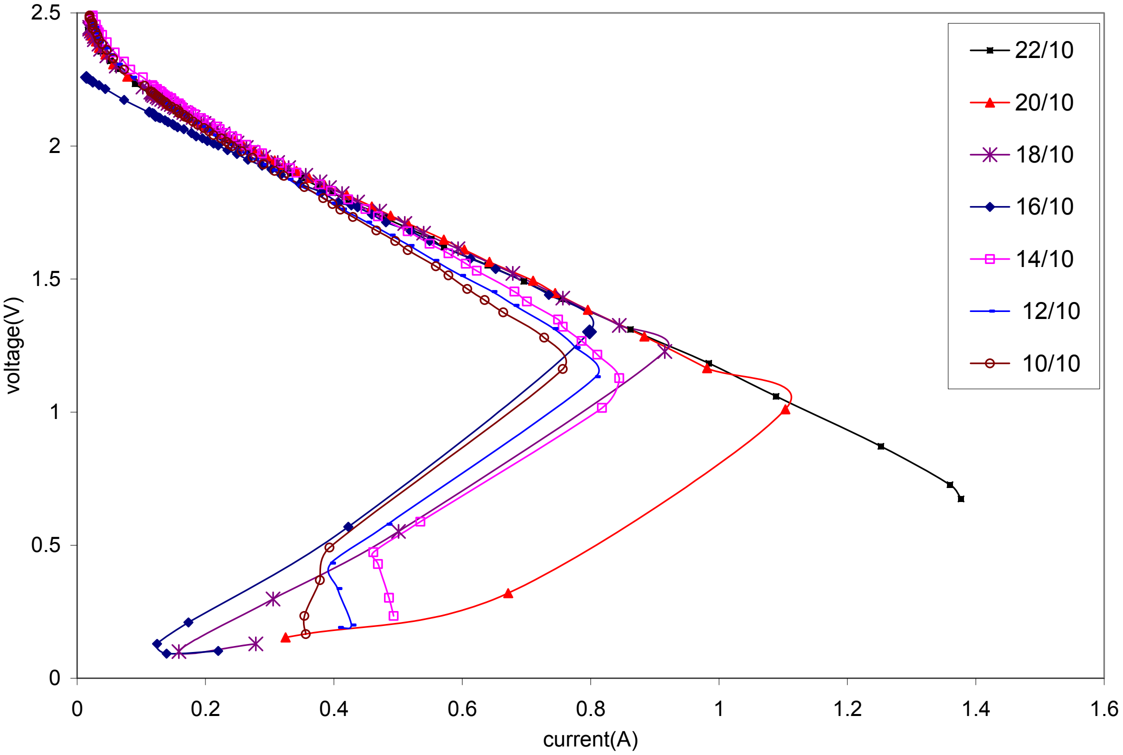

Figure 4.11 IV curves obtained after equilibration of three-cell stack at 3 Ω and 60°C at different H_2/O_2 flow rates. In all flow conditions besides 22/10 mL/min H_2/O_2 feeds, starvation was observed at low loads when current experienced a reversal in trend and decreased. For all flow conditions, maximum current attained was actually higher than expected if 100% H_2 utilization achieved, which was a result of the H_2 reservoir in gas flow channels. The same phenomenon had been observed in the 2-cell stack. This is equivalent to a capacitor in an electric circuit, which reduces the response time to load changes.

Figure 4.11 shows the IV curves obtained at different H_2/O_2 flow rates after equilibration at 60°C and 3 Ω load. At all flow conditions studied, the maximum current obtained during the IV sweep was larger than the theoretically calculated maximum if reactants had been equally distributed among the 3 cells and completely utilized. The comparison is shown in Table 4.8. As explained in Section 4.1.1, this was due to the existence of reactant reservoirs in the fuel cell. The extra H_2 stored in the gas flow channels provided the fuel for current generation despite the lower supply from the feed flow. However, this larger current could not be sustained for long periods of time since H_2 stored would eventually run out. This was manifested in the sudden reversal of performance at low loads where current quickly decreased.

H_2/O_2 flow [mL/min]	H_2 feed [mol/min]	O_2 feed [mol/min]	Theoretical i_{max} at 100% utilization [A]	Max current during IV sweep [A]
22/10	8.88e-04	4.04e-04	0.87	1.38
20/10	8.07e-04	4.04e-04	0.87	1.10
18/10	7.27e-04	4.04e-04	0.78	0.92
16/10	6.46e-04	4.04e-04	0.69	0.81
14/10	5.65e-04	4.04e-04	0.61	0.84
12/10	4.84e-04	4.04e-04	0.52	0.81
10/10	4.04e-04	4.04e-04	0.43	0.76

Table 4.8 Comparison of theoretical i_{max} if 100% reactant utilization were achieved and maximum current obtained during fast IV sweeps. The larger current obtained during the fast IV sweep was due to a net depletion of H_2 stored in gas flow channels, which added a capacitance element to the fuel cell stack. The maximum amount of H_2 stored in the gas flow channels was 2.38e05mol, which could theoretically generate 4.6 coulombs of charge. This would correspond to a current level of 1.5A in 3 seconds.

It is perhaps more helpful to look at results of a specific flow rate for further analysis. Figure 4.12 shows the IV curve of each individual cell as well as the total voltage of the stack at 12/10 flow. As the load was decreased from 110Ω to 1.4Ω, current steadily increased from 0A to 0.81A. The maximum current of 0.81A obtained was much larger than the theoretically possible limit of 0.52A calculated from a H_2 mole balance. However, as the load was reduced further, current experienced a sudden reversal and decreased to a value below the theoretically limit of 0.52A instead of continuing the steady accent.

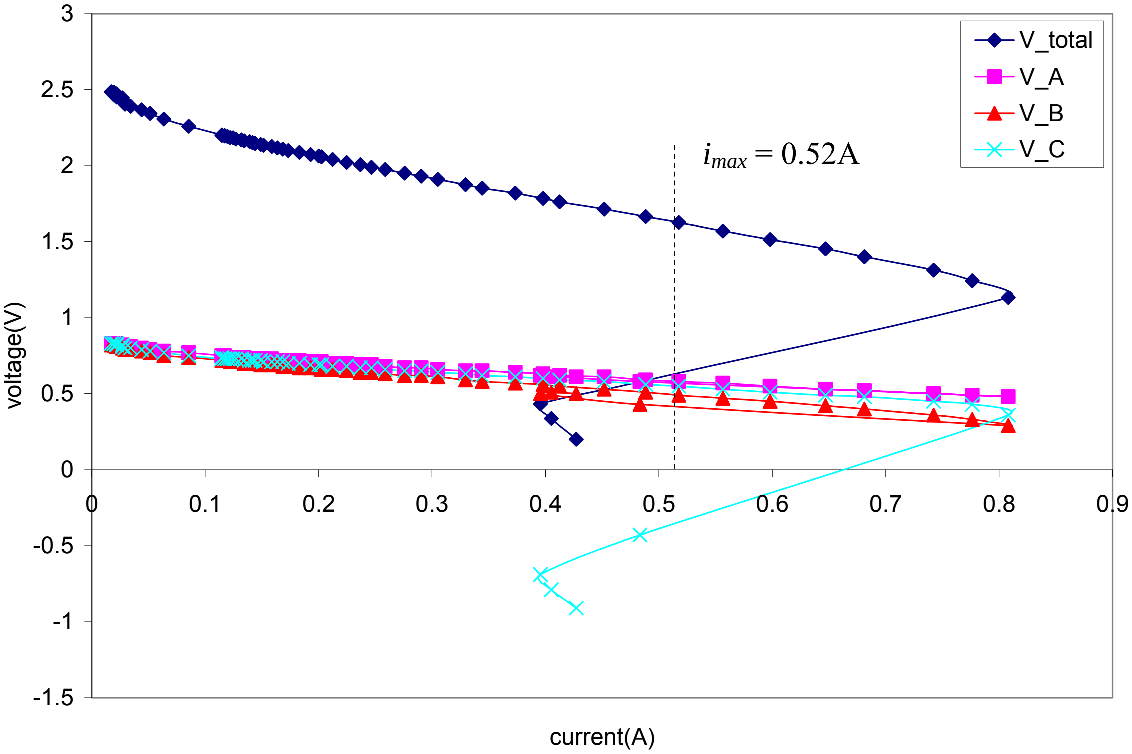

Figure 4.12 IV curves of individual cells at 12/10 H_2/O_2 flow at 60°C after equilibration at 3 Ω load. As indicated by the dotted line on the figure, the current obtained during this fast IV sweep was much larger than the theoretical limit of 0.52A (if all the H_2 fed was evenly divided among the 3 cells and was completely reacted). The larger current obtained was due to usage of extra H_2 stored in gas flow channels. At high current, cell A and cell B were using up most of the hydrogen being fed to the stack, so cell C entered starvation condition much sooner, indicated by the sudden sharp decrease in V_C. The trend was consistent at other H_2 flow rates.

A closer look at individual voltages revealed a possible explanation for current reversal. First of all, in the ohmic region of the curve where load was higher than 1.4Ω, cell B maintained a lower voltage than cell A and cell C, which was consistent with steady-state results shown in Table 4.7. Then as the load was reduced, current was expected to increase, but in reality, there was not enough fuel being supplied to the stack. Most of the H_2 supplied was distributed to cell A and cell B, and little H_2 was reaching the downstream cell C. Cell C was starved of H_2, which could explain the large decrease in V_C shown in Figure 4.12. In other words, before the U-turn in current, cell C generated more than 0.52A of current for 8 seconds by using the H_2 stored in the gas flow channels, but as the H_2 reservoir was depleted, the amount of H_2 delivered to cell C limited the amount of current that could be generated. In short, the capacitance of the stack made it possible for the stack to reach a higher current than the theoretical limit but the depletion of the reservoir caused the interesting current reversal phenomenon during the IV sweep of the three-cell stack. At low loads, the amount of H_2 available to cell C essentially limited the maximum current that could be generated by the stack.

4.3 Long Term Stability of the Three-cell Stack

All the results presented so far involved tests that at most lasted for 4 hours. But fuel cells must be able to operate for long hours in order to be useful. To investigate long-term stability, the 3-cell stack was operated at 60°C and 3Ω load for 36 hours with H_2/O_2 flow at 18/10 mL/min. As shown in Figure 4.13, current and total voltage started at 0.52A and 1.58V but decreased over 12 hours and stabilized at 0.45A and 1.35V respectively.

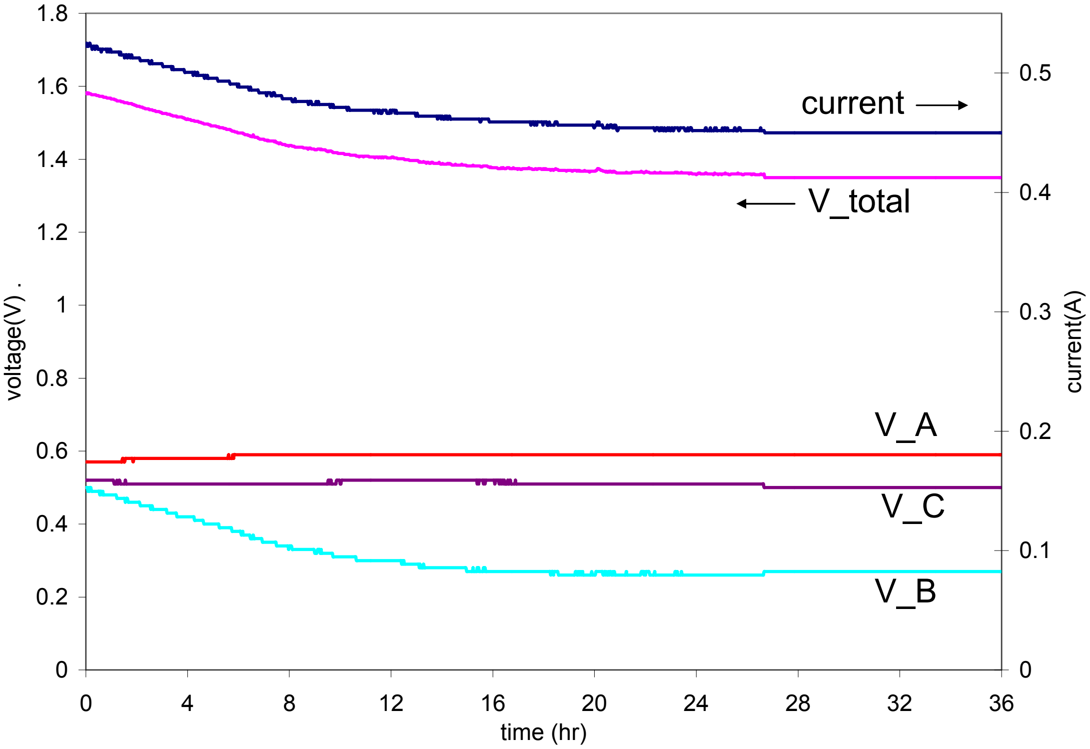

Figure 4.13 Long-term performance of 3-cell stack at 60^0C, 3Ω, and 18/10 H_2/O_2 flow. Current and total voltage decreased over time mainly due to a decline in cell B performance. Voltage in cell A and cell C remained mostly constant over the entire test. The drop in V_B was probably due to difficulty in water drainage from cell B, thus leading an increase in $R_{int,B..}$ This observation coincided with earlier tests in the three-cell stack where cell B always had a reduced performance compared to cell A and cell C. At steady-state, 58% H_2 and 52% O_2 were utilized.

A closer look at individual cell voltages revealed that the decrease in voltage was mainly due to a reduction in V_B. V_A and V_C remained more or less constant at 0.59V and 0.50V respectively over the entire test period. On the other hand, V_B decreased significantly from 0.50V to 0.27V. Assuming that the battery voltage of cell B remained constant at about 0.8V over this period, the internal resistance can be calculated from Equation 4.2, which was derived from Equation 2.3.

$$R_{\text{int}} = \frac{V_b - V}{i} \tag{4.2}$$

This yields an increase in $R_{\text{int,B}}$ from 0.58 Ω to 1.18Ω, which is more than doubling over a 12-hour period. If the increase in internal resistance was mainly due to flooding, it meant the active area of the membrane decreased by more than half during this period. In other words, half the gas flow channels or gas diffusion layer in cell B could have been blocked. At steady-state, water level in anode and cathode should be the same since water diffusion would eliminate any concentration gradient. If water filled half the volume of gas flow channels in both the anode and cathode, this would mean about 0.82mL of liquid water was trapped in cell B. Water drainage from cell B was expected to be more difficult because it is situated in the middle of the stack where there are no downward-sloping exit channels on either side of the cell. This is a problem that should be addressed in the next generation of stack design.

4.4 A Study on Water Removal and Water Collection at Outlets

Prolonged operation of the 3-cell stack generated enough water to allow a comparison of water collected at the outlets and the water produced by the reaction. Table 4.9 provides a summary of the results for 18/10 H_2/O_2 flow at 60°C and 3Ω load. Over a 36-hour period, a total of 7.7mL of water was collected at the outlet water baths - 6mL at the H_2 outlet and 1.7mL at the O_2 outlet. It is surprising that less water was collected at the O_2 outlet despite the fact that water was being generated at the cathode catalyst surface. This was probably because the total flux of oxygen through the fuel cell was smaller than the total flux of hydrogen at 18/10 flow. Table 4.9 shows the H_2 and O_2 exit flow rates calculated from a mole balance. At steady-state where all unreacted gas should the stack and assuming minimal crossover, H_2 exit flow rate was 8.1mL/min and O_2 exit flow rate was 5.1mL/min. Thus, liquid water was expected to be swept out of the anode at a faster rate.

18/10 H_2/O_2 flow at T_{stack} = 60°C and R_L = 3Ω	
Total duration	36 hour
Water collected at H_2 outlet	6.0 mL
Water collected at O_2 outlet	1.7 mL
Total water collected	0.43 mol (7.7 mL)
Average H_2 exit flow rate	17400 mL(or 8.1 mL/min)
Average O_2 exit flow rate	11100 mL (or 5.1 mL/min)
Water convectively removed	0.21 mol (3.7mL liquid)
Average current	0.47 A
Water produced in 1 cell	0.31 mol
Water produced in 3 cells	0.93 mol (16.9mL)

Table 4.9 Amount of water collected, generated, and convectively removed at operating conditions of 18/10 flow, 60°C, and 3Ω. Due to higher H_2 exit flow, significantly more water was collected at the H_2 outlet than at the O_2 outlet. Water collected at outlet water baths was less than half of what should have been produced from the reaction. Some water was removed convectively by unreacted gas. Water could also be trapped in cell B and in channels interconnecting the individual cells.

In comparison, at 14/10 flow where H_2 and O_2 exit flow rates were more similar, the amount of water collected at the two outlets became more similar. Table 4.10 shows that for 14/10 flow condition, H_2 exit flow rate was 5.7mL/min and O_2 exit flow rate 6.2mL/min. And 3.7mL and 2.7mL of liquid water were collected at the anode and cathode respectively. This observation suggests that back-diffusion of water from cathode catalyst layer to the anode was relatively fast. Moreover, water removal from the stack by gas convection is the dominant process of water management in this system, and this convective transport is highly dependent on gas flow rate in the stack.

14/10 H_2/O_2 flow at $T_{stack} = 60^oC$ and $R_L = 3\Omega$	
Total duration	36 hour
Water collected at H_2 outlet	3.7 mL
Water collected at O_2 outlet	2.7 mL
Total water collected	0.35 mol (6.4 mL)
Average H_2 exit flow rate	12300 mL (or 5.7 mL/min)
Average O_2 exit flow rate	13400 mL (or 6.2 mL/min)
Water convectively removed	0.19 mol (3.4 mL liquid)
Average current	0.38 A
Water produced in 1 cell	0.26 mol
Water produced in 3 cells	0.78 mol (14.0 mL)

Table 4.10 Amount of water collected, generated, and convectively removed at operating conditions of 14/10 flow, 60°C, and 3Ω. The amount of water collected at H_2 and O_2 was more comparable as H_2 and O_2 exit flow rates were more similar than in the case of 18/10 flow shown in Table 4.9. Similar to 18/10 flow, liquid water collected was less than half of what should have been produced from the reaction. Some water was removed convectively by unreacted gas and some could be trapped in channels connecting individual cells.

At 18/10 flow, an average current of 0.47A was generated over the 36-hour period. This should theoretically have produced 0.31 moles of water in 1 cell. Since this was a three-cell stack, a total of 0.93 moles of water should have been produced. If all of this water condensed at the outlet water baths, 16.9mL liquid water should have been collected. This was more than double the actual amount of 7.7mL collected. Similarly, at 14/10 flow, an average of 0.38A current should have generated 14.0mL of liquid water in the three-cell stack but only 6.4mL was collected over a 36-hour period.

Where did half of the water go? One obvious loss was water carried away by unused reactants exiting in the form of gas bubbles. Assuming that unreacted H_2 and O_2

leaving the system were completely saturated at 60°C, they could potentially carry off 0.21mol of water (3.7mL liquid) at 18/10 flow and 0.19mol of water (3.4mL liquid) at 14/10 flow (calculations shown in Table 4.9 and 4.10). To test the assumption that gases leaving the water baths were saturated at 60°C, the stack was operated at 25°C with 14/10 flow for 18 hours. The vapor pressure of water is 0.03bar at 25°C and 0.2bar at 60°C. This means at 25°C, the gases could hold much less water and more liquid water should be collected. Table 4.11 summarizes the results of water balance at stack operating temperature of 25°C. The total amount of water collected at the outlets was 3.5mL, which accounted for up to 83% of the 4.2mL of water that should have been produced by the reaction. About 0.022 moles should have been convectively removed at this temperature, which would correspond to about 0.4mL of liquid water. This supports the hypothesis that at high operating temperature, more water was removed convectively by exit gas due to higher vapor pressure of water.

14/10 H_2/O_2 flow at $T_{stack} = 25^oC$ and $R_L = 3\Omega$	
Total duration	18 hour
Water collected at H_2 outlet	3.2 mL
Water collected at O_2 outlet	0.3 mL
Total water collected	0.19 mol (3.5 mL)
Average H_2 exit flow rate	9300 mL (or 8.6 mL/min)
Average O_2 exit flow rate	7900 mL (or 7.3 mL/min)
Water convectively removed	0.022 mol (0.4 mL liquid)
Average current	0.23 A
Water produced in 1 cell	0.078 mol
Water produced in 3 cells	0.23 mol (4.2 mL)

Table 4.11 Amount of water collected, generated, and convectively removed at operating conditions of 14/10 flow, 25°C, and 3Ω. Unlike operation at 60°C, amount of water collected at outlet corresponded much more closely to total water generated by reaction. This supported the hypothesis that at high operating temperature, due to high vapor pressure of water, more water vapor remained in exit gas and thus less liquid water was collected. At this operating temperature, up to 83% of the water condensed and was collected at the outlet.

Besides convective transport, some water could have been trapped in the stack, particularly in cell B which experienced a decrease in voltage over the test period. As mentioned in Section 4.3, if half of the gas flow channels in both the anode and cathode of cell B were blocked at 18/10 flow, it could account for 0.82mL of water. In addition, water could have been trapped in the channels connecting the individual cells, a phenomenon shown in Figure 4.7. The original single STR fuel cell was able to drain water very well because it did not have any horizontal surfaces and thus gravity facilitated water removal. However, horizontal surfaces were introduced when the single cell was expanded into a stack, particularly in the channels connecting the individual cells. This led to easy water buildup, and results so far had demonstrated that this had drastic effects on stack performance.

4.5 Current Control by Hydrogen Starvation in the Three-cell Stack

Output current control by H_2 starvation was attempted in the 2-cell stack at operating conditions of 60°C, a constant load of 2Ω, and excess O_2 feed of 8mL/min. Equation 2.12 was used as the governing equation during optimization of control parameter. Current was successfully controlled for short durations. However, as anticipated in previous sections, several problems arose when H_2 was starved, including instabilities caused by flooding and extinction of downstream cell.

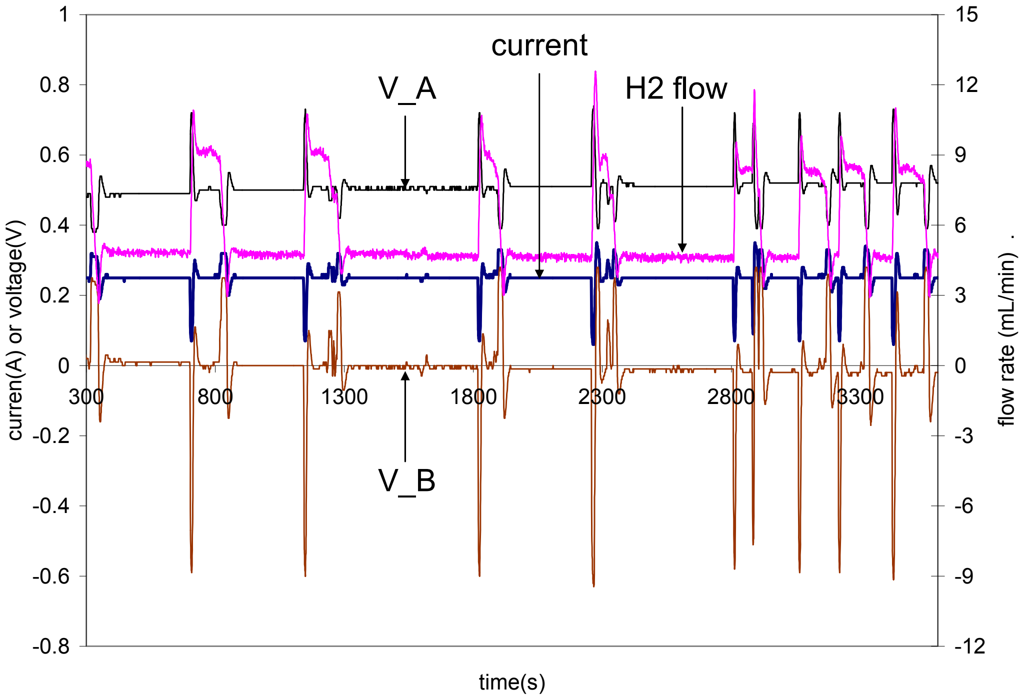

Figure 4.14 Two-cell stack performance during output current control by H_2 starvation at 60°C and constant 2Ω load. O_2 was fed in excess at flow rate of 8mL/min. Current setpoint was 0.25A. The longest stable period where control was maintained was 507s (≈ 8.5minutes). On average, about every 5 minutes, V_B would drop whereas V_A would increase. This would be accompanied by a current drop. Then H_2 flow would increase quickly in response, and the stack would recover in about 30 seconds. Greater detail is shown in Figure 4.15.

Figure 4.14 shows the transient response of the two-cell stack under current control by H_2 starvation. Despite periodic drops and spikes, current was able to return to the setpoint value of 0.25A. The longest stable period was about 507s (≈ 8.5 minutes). On average, every 5 minutes or so, V_B would drop from zero to negative values whereas

V_A would increase from 0.5V to higher values. At the same time, current would drop to 0.05A. Then H_2 flow would increase quickly in response, and the stack would recover in about 30 seconds, as shown in greater detail in Figure 4.15. However, within this 30-second period, H_2 flow would settle at an excess value (≈ 9mL/min). There was a lag time of about 50s before current would increase to a larger value that corresponded to the higher H_2 flow rate. As current increased and crossed the setpoint, H_2 flow would decrease slowly to previous level, which would cause the current to fall back down to the setpoint value again. This whole cycle took about 120s. This instability could have been due to water buildup in the stack. Slight changes in water level would vary the amount of fuel delivered to cell B, causing big changes in V_B. Future work is required to examine detailed dynamics and determine the explanation for such instabilities.

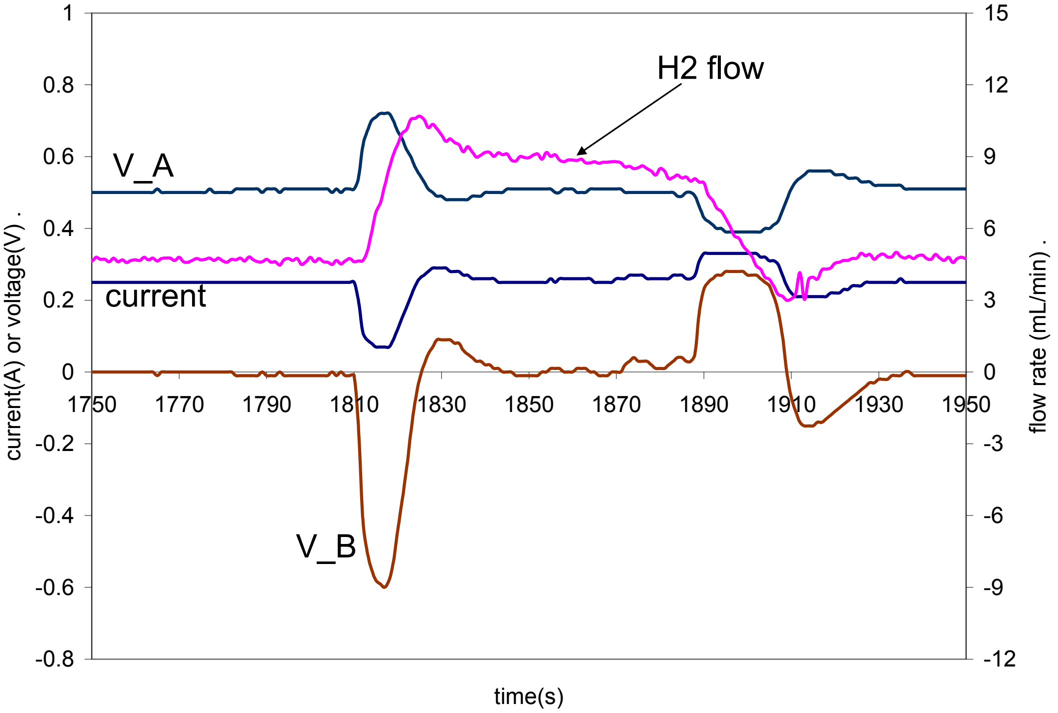

Figure 4.15 Detailed responses in current, voltage, and H_2 flow rate during current control by H_2 starvation in the two-cell stack within 200s of instability (excerpt from t = 1750s to 1950s of Figure 4.14). Current drop was accompanied by a drop in V_B and a rise in V_A. H_2 flow increased and settled at an excess flow rate until current rose to above setpoint value of 0.25A. Then the control program would reduce H_2 flow and lead to a slow decrease of current back to setpoint value.

During the stable periods, average H_2 flow was 4.64 mL/min. To produce 0.25A current in 2 cells, theoretical H_2 flow needed was 4.30 mL/min, so 93% H_2 utilization was achieved. Table 4.12 shows the average H_2 flow rate and % H_2 utilization at different setpoint currents. For 3 different setpoint currents, more than 90% H_2 utilization was possible, although stability could not be maintained for more than 500 seconds at a time. Transient stack response at different current setpoints is also shown in Figure 4.16. In addition, Table 4.13 shows that at lower currents, the gap between cell A and cell B voltage became larger. This suggests that cell B was limiting the current and was essentially the bottleneck of the overall system.

Setpoint Current [A]	H_2 used in 2 cells [mol/min]	Average H_2 supply [mol/min]	H_2 Utilization [%]	V_A [V]	V_B [V]
0.3	2.08E-04	2.15E-04	97	0.45	0.15
0.25	1.74E-04	1.87E-04	93	0.5	0.0
0.2	1.39E-04	1.51E-04	92	0.57	-0.18
0.15	1.04E-04	1.47E-04	71	0.59	-0.29

Table 4.12 Average H_2 supply and % utilization in two-cell stack during current control by H_2 starvation at 60°C and a constant 2Ω load. Higher % utilization was achieved at higher setpoint current. Note that V_B was consistently smaller than V_A. There was also a larger discrepancy between V_A and V_B at lower current and H_2 flow rate. The starved cell B set the limit on current generated, which made control by fuel starvation partly possible.

These results demonstrated that during current control by hydrogen starvation although near 100% H_2 utilization was achieved, current was not able to remain stable for longer than 5-8 minutes due to gas flow and/or water management problems. In fact, these are similar problems encountered in large fuel cell stacks. Most commercial fuel cells have serpentine flow channels that are akin to plug flow reactors. High stoichiometry is used in these serpentine flow channel fuel cell stack in order to ensure that downstream cells get enough reactants to avoid starvation. This operating condition also avoids flooding since high-velocity gas pushes out any liquid water condensed in the channels. Although the stack being studied here only consisted of 2 or 3 cells connected in series (i.e. 2 or 3 coupled stirred tank reactors), the system was able to emulate some of the operational problems in large fuel cell stacks that are similar to plug flow reactors.

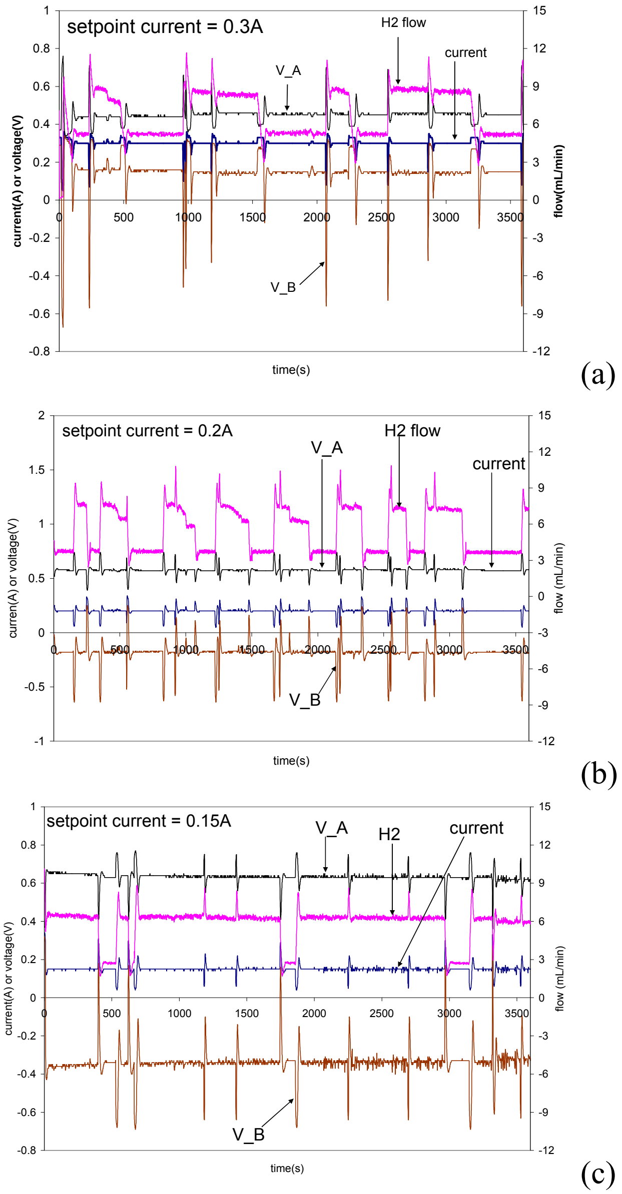

Figure 4.16 Stack performance under H_2 starvation control at other setpoint currents for 1hour each. Current setpoint was 0.3A in (a), 0.2A in (b), and 0.15A in (c).

4.6 Comparison of Graphite and Stainless Steel as Bipolar Plate Material

The IV curves shown in Figure 4.17 illustrate the reduced performance of the stainless steel stack compared to the graphite stack at the same operating temperature of 60°C and 10/5 H_2/O_2 feed. Although the open circuit voltages were similar, ohmic losses were much larger in the stainless steel stack, which meant internal resistance was larger. R_{int} for the graphite stack was 2.33Ω, whereas R_{int} for the stainless steel stack was 2.97Ω.

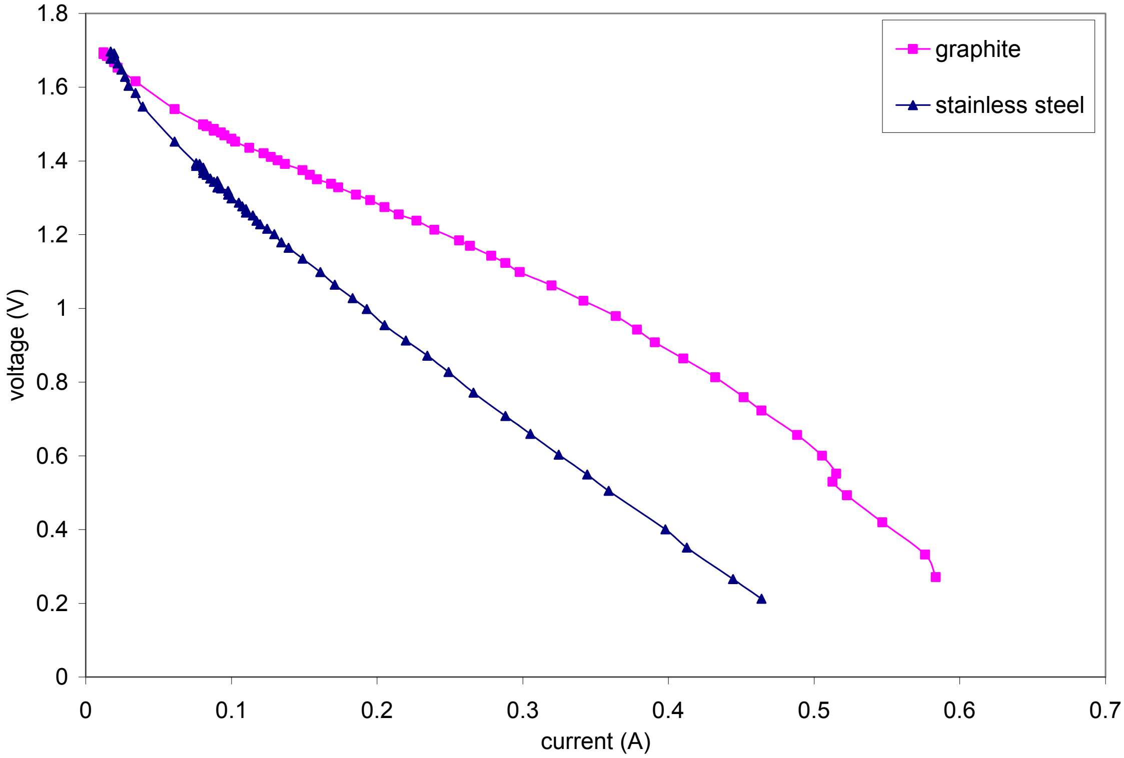

Figure 4.17 IV curves comparing performance of graphite stack and stainless steel stack at H_2/O_2 flow of 10/5 mL/min and 60°C after equilibration at 2Ω. R_{int}, calculated from the negative slope of the ohmic region is 2.33Ω for the graphite stack and 2.97Ω for the stainless steel stack. The larger R_{int} in stainless steel stack was likely caused by flooding in gas flow channels due to water build-up on stainless steel surface.

When the stainless steel bipolar plates were inspected after testing, considerable amount of water droplets were always seen on the stainless steel surface. More than 30% of the surface area of the gas flow channels in both the anode and cathode were covered by liquid water. This was never observed in the graphite stack. Thus, water blockage of gas flow channels and gas diffusion layers in the stainless steel stack was probably the cause of the larger R_{int} due to reduced active membrane area.

Stainless steel has a wetting surface whereas graphite has a non-wetting surface. This means the interfacial attraction of water and stainless steel is much larger than that between water and graphite. In other words, the self-draining design of the STR fuel cell became ineffective with stainless steel. In addition, the decreased depth of gas flow channels in the stainless steel stack made them more susceptible to flooding (see Figure 3.4), which resulted in a decrease in active membrane area and thus an increase in internal resistance.

In addition to the IV curves, steady-state current of the stainless steel stack was also worse than that of the graphite stack. As shown in Table 4.13, at 12/10 flow, the graphite stack achieved a current of 0.39A whereas the stainless steel stack could only output 0.34A. At lower feed flow rates, the discrepancy in the performance of the 2 stacks was even larger. This was probably because even less water could be removed convectively by exit gases and flooding was exacerbated as water accumulated on the wetting surface of the stainless steel plates.

	Stainless steel stack				Graphite stack			
H_2/O_2 [mL/min]	Current [A]	V_{total} [V]	V_A [V]	V_B [V]	Current [A]	V_{total} [V]	V_A [V]	V_B [V]
12/6	0.34	0.69	0.42	0.27	0.39	0.78	0.42	0.37
10/8	0.19	0.38	0.42	-0.04	0.42	0.84	0.47	0.37
10/5	0.19	0.38	0.58	-0.21	0.38	0.76	0.38	0.38

Table 4.13 Comparison of steady-state performance of stainless steel stack and graphite stack. At all flow rates, the stainless steel stack produced less current and power. The inferior performance was likely due to the blockage of narrower gas flow channels by water build-up on the wetting surface of stainless steel.

Bipolar plates are crucial for distributing reactants and carrying water away from the fuel cell. Considerations in material selection include resistance to corrosion, cost, density, electrical conductivity, gas impermeability, manufacturability, and thermal conductivity. One of the disadvantages of graphite was its permeability to gases, which led to the investigation of stainless steel as an alternative material. According to most literature, stainless steel is not a suitable material for bipolar plates due to corrosion at low pH conditions at the anode, although this can be overcome by coating it with graphite, conductive polymer, or noble metals [28]. Although corrosion was not observed in the system under study, results shown above have demonstrated an additional disadvantage of stainless steel. Its wetting property makes the draining of water from gas flow channels difficult. This exacerbates the problem of flooding and reduces the overall performance of the fuel cell. The high density of stainless steel also makes it less attractive for transportation and space applications which prefer lighter materials.

One other purpose of bipolar plates is to help keep the fuel cell cool, so the material should be able to remove heat effectively, especially in a large stack where heat generated by the reaction needs to be dissipated to prevent reaction run-off. This means a higher thermal conductivity is better. Graphite, which has a higher thermal conductivity of 24 W/m-K compared to 16.3 W/m-K of stainless steel, is thus favored.

5. Conclusions

5.1 Behavioral Trends and Operational Difficulties in the STR Fuel Cell Stack

This thesis expanded the STR design of a single PEM fuel cell into a stack and examined the transient and steady-state dynamics of the stack at various flow rates of hydrogen and oxygen feeds. For the two-cell stack, a vacuum was created near the outlet at starvation condition, causing water to be pushed into the cell by the larger atmospheric pressure. Water blocked active membrane area and led to increase in internal resistances. In addition, imperfect drainage system in the stack led to easy buildup of water in gas flow channels, which was a potential cause of instabilities observed at low flow rates when liquid water removal by gas convection was limited. Non-uniform distribution of reactants also limited the maximum current that could be generated by the stack. The existence of reactant reservoirs in the STR fuel cell created an equivalent capacitance element which slowed down the response of the fuel cell to load changes.

The three-cell stack exhibited similar behavioral trends. The problem of flooding was worst in the middle cell which did not have downward-sloping outlet channels to facilitate water removal. Uneven reactant distribution led to early starvation of a downstream cell, which then became a bottleneck in the system and limited the overall stack performance.

Long-term stability of the three-cell stack was demonstrated at excess hydrogen and oxygen feeds, but it took more than 10 hours for the three-cell stack to reach steady-state due to the slow accumulation of water in the middle cell which experienced a gradual reduction in performance over time. A water balance of the system during long-term operations demonstrated that diffusion of water across the electrodes was fast, and water removal by exit gas was the dominant process for water management in the system. The effect of temperature was also important due to the heavy dependence of water vapor pressure on temperature. At lower operating temperature, more liquid water condensed, which could potentially lead to instabilities in the stack.

Feasibility of current control by fuel starvation was only partially successful in the two-cell stack. Although near 100% utilization was achieved, the stack could only remain stable at the setpoint current for about 5 minutes at one time. Uneven reactant distribution and water buildup were two main problems identified during fuel starvation. These also happened to be some of the same operational difficulties in large commercial fuel cell stacks.

5.2 Stainless Steel as Bipolar Plates

The stainless steel stack demonstrated reduced performance compared to the graphite stack because of the wetting property of stainless steel. The larger interfacial attraction between water and stainless steel made it difficult for water to drain from the fuel cell. Gas flow rates employed were also not large enough to convectively remove liquid water stuck to the stainless steel surface.

5.3 Future Work

The two main problems identified in the STR stack design were water management and reactant distribution. Future work should focus on monitoring water transport in the fuel cell stack. The effect of temperature should also be investigated. Operating the fuel cell stack at room temperature is expected to lead to reduced performance and increased instability since more water will condense. The effect of substituting oxygen with air should also be examined since most commercial fuel cells operate with air instead of pure oxygen.

Stack performance can probably be improved by getting rid of horizontal surfaces in the stack. A schematic of suggested design modifications is shown in Figure 5.1. In this design, the connecting channels are slanted to make use of gravity to facilitate liquid water drainage. The outlet channels from cell A and cell C slope down and converge in the middle. This design also shows inlet gas flowing into the middle of the stack where the gas is then distributed to the individual cells. This should lead to more uniform distribution of reactants by careful sizing of each channel. With this modified design, careful balance of water production and water removal by gas convection can potentially improve stability at low flow rates and lead to successful control by fuel starvation.

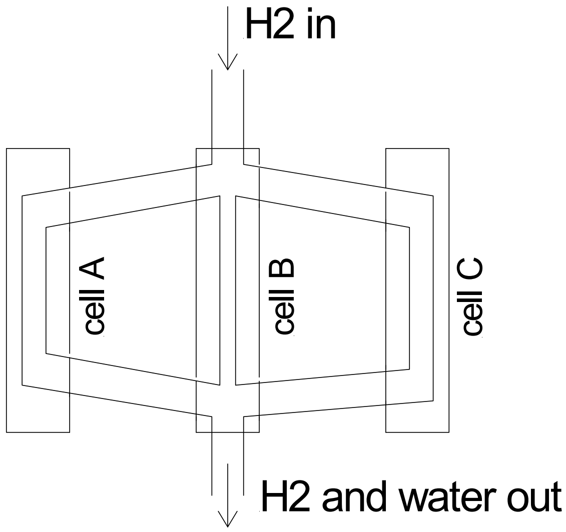

Figure 5.1 A modified stack design that could potentially lead to better water drainage and more uniform gas distribution.

References

1. EG&G Services, *Fuel Cell Handbook*, 5th Edition. Parsons Inc. October 2000.
2. S.Gottesfeld, T.Zawodinski, Polymer electrolyte fuel cells, *Advances in Electrochemical Science and Engineering*. **5** (1997) 195-301.
3. K. Sopian, and W.R. Wan Daud. Challenges and Future Developments in Proton Exchange Membrane Fuel Cells. *Renewable Energy* **31**, 2006, 719-727.
4. Pukrushpan, J.; Stefanopoulou A.G.;and Peng H.. Control of Fuel Cell Breathing, *IEEE Control Systems Magazine,* 2004. 30-46.
5. Suh, K.W. and Steganopoulou, A.G. Coordination of Converter and Fuel Cell Controller. *International Journal of Energy Research*, **29**, 2005. 1167-1189.
6. Sun, J. and Kolmanovsky, I. Load Governor for Fuel Cell Oxygen Starvation Protection: A Robust Nonlinear Reference Governor Approach, *IEEE Transactions on Control Systems Technology*, **13** (6), 2005. 911-920.
7. Wilkinson D.P. and Vanderleeden O. *Handbook of Fuel Cells,* W. Vielstich, H. Gasteiger, and A. Lamm, Editors. 2003, Wiley: England. p.315-324.
8. Larminie J. and Dicks A. *Fuel Cell Systems Explained, 2nd Edition,* Wiley, New York, 2003.
9. Yu, X., Zhou B. and Sobiejak A. Water and Thermal Management for Ballard PEM Fuel Cell Stack, *Journal of Power Sources*, **147**, 2005, 184-195.
10. Natarajan, D. and Nguyen T.V. Current Distribution in PEM Fuel Cells. Part 1: Oxygen and Fuel Flow Rates Effects, *AIChE Journal*, 2005. **51** (9): 2588-2598.
11. Scholta J et al. Development and Performance of a 10kW PEMFC Stack. *Journal of Power Sources*, **127**, 2004, 206-212.
12. Giddey S., Ciacchi, F.T.; and Badwal, S.P.S. Design, Assembly and Operation of Polymer Electrolyte Membrane Fuel Cell Stacks to 1kW$_e$ Capacity, *Journal of Power Sources*, **125**, 2004, 155-165.
13. Nguyen T.V. and Knobbe, M.W. A Liquid Water Management Strategy for PEM Fuel Cell Stacks, *Journal of Power Sources*, **114**, 2003, 70-79.
14. Watanabe et al. Self-humidifying Polymer Electrolyte Membranes for Fuel Cells. *Journal of the Electrochemical Society*, **143** (12), 1996, 3847-3852.
15. Ge, S., Li, X., and Hsing I. Internally Humidified Polymer Fuel Cells Using Water Absorbing Sponge, *Electrochimica Acta*, **50**, 2005, 1909-1916.
16. Buchi F.; Srinivasan S. Operating Proton Exchange Membrane Fuel Cells Without External Humidification of the Reactant Gases. *Journal of Electrochemical Society*, **144** (8), 1997, 2767-2772.
17. Qi, Z., and Kaufman, A. PEM Fuel Cell Stack Operated under Dry-Reactant Conditions, *Journal of Power Sources*, **109**, 2002, 469-476.
18. Benziger et al. The Stirred Tank Reactor Polymer Electrolyte Membrane Fuel Cell, *AIChE Journal*, **50** (8), 2004, 1889-1990
19. Pukrushpan, J.; Stefanopoulou A.G.; and Peng H. Modeling and Control for PEM Fuel Cell Stack Systems, *Proceedings of the American Control Conference*, 2002. 3117-3122.
20. Lauzze, K.C, and Chmielewski, D.J., Power Control of a Polymer Electrolyte Membrane Fuel Cell, *Industrial and Engineering Chemistry Research*, 2005. submitted.

21. Golbert, J. and Lewin D.R. Model-based Control of fuel cells: (1) Regulatory control, *Journal of Power Sources* **135**, 2004. 135-151.
22. Pukrushpan et al. Control-Oriented Model of Fuel Processor for Hydrogen Generation in Fuel Cell Applications. *Control Engineering Practice*, **14**, 2006, p.277-293.
23. Song R-H, Kim C-S, Shin D.R. Effects of Flow Rate and Starvation of Reactant Gases on the Performance of Phosphoric Acid Fuel Cells. *Journal of Power Sources*, **86**, 2002, 289-293.
24. Benziger et al. The Power Performance Curve for Engineering Analysis of fuel cells, *Journal of Power Sources*, **155**, 2006, 272-285.
25. Jeng et al. Oxygen Mass Transfer in PEM Fuel Cell Gas Diffusion Layers, *Journal of Power Sources*, **138**, 2004, 41-50.
26. Moxley, J., Tulyani S., Benziger J. Steady-State Multiplicity in the Autohumidification Polymer Electrolyte Membrane Fuel Cell. *Chemical Engineering Science*, **58**, 2003, 4705-4708.
27. Taniguchi et al. Analysis of Electrocatalyst degradation in PEMFC Caused by Cell Reversal during Fuel Starvation. *Journal of Power Sources*, **130**, 2004, 42-49.
28. Mehta V. and Cooper J.S. Review and Analysis of PEM Fuel Cell Design and Manufacturing, *Journal of Power Sources*, **114**, 2003. 32-53.